HAL
archives-ouvertes.fr

NURBS-based Isogeometric analysis of standard and phase reduction On-Surface Radiation Condition formulations for acoustic scattering

Xavier Antoine, Tahsin Khajah

▶ **To cite this version:**

Xavier Antoine, Tahsin Khajah. NURBS-based Isogeometric analysis of standard and phase reduction On-Surface Radiation Condition formulations for acoustic scattering. 2021. hal-03167068

HAL Id: hal-03167068
https://hal.archives-ouvertes.fr/hal-03167068

Preprint submitted on 11 Mar 2021

HAL is a multi-disciplinary open access archive for the deposit and dissemination of scientific research documents, whether they are published or not. The documents may come from teaching and research institutions in France or abroad, or from public or private research centers.

L'archive ouverte pluridisciplinaire **HAL**, est destinée au dépôt et à la diffusion de documents scientifiques de niveau recherche, publiés ou non, émanant des établissements d'enseignement et de recherche français ou étrangers, des laboratoires publics ou privés.

NURBS-based Isogeometric analysis of standard and phase reduction On-Surface Radiation Condition formulations for acoustic scattering

Xavier ANTOINE[1] and Tahsin KHAJAH[2]

Abstract

This paper is devoted to the NURBS-based Isogeometric analysis of the On-Surface Radiation Condition (OSRC) method for solving two- and three-dimensional time-harmonic acoustic scattering problems. In addition, a Phase Reduction of the OSRC formulation based on a plane wave ansatz is introduced. This leads to an efficient and accurate implementation of OSRC methods. Some numerical tests for two- and three-dimensional problems illustrate the proposed approach.

Keywords: acoustic scattering; on-surface radiation condition; isogeometric analysis; Non Uniform Rational B-Splines; phase reduction

Contents

1 Introduction **2**

2 OSRC and PR-OSRC formulations **3**
2.1 The time-harmonic scattering problem 3
2.2 The OSRC method and its standard formulation 3
2.3 Phase Reduction OSRC formulation (PR-OSRC) 6

3 IGA approximation of OSRC formulations **8**
3.1 A brief overview of IGA 8
3.2 Computation of geometrical features in IGA for OSRC 9
3.3 IGA approximation of the OSRC and PR-OSRC formulations 10

4 Numerical example: two-dimensional scattering by a disk **11**
4.1 Padé parameters for IGA-OSRC 11
4.2 Accuracy of IGA-OSRC and IGA-PR-OSRC 12

5 Scattering by a submarine-like shaped scatterer **16**

[1]Université de Lorraine, CNRS, Inria, IECL, F-54000 Nancy, France.
Email: xavier.antoine@univ-lorraine.fr
[2]Department of Mechanical Engineering, University of Texas at Tyler, USA.
Email: tkhajah@uttyler.edu

6 Three-dimensional scattering 19

7 Conclusion 23

1. Introduction

The numerical solution of high frequency time-harmonic acoustic, electromagnetic and elastic wave scattering problems is very challenging in computational science because of its importance in numerous technological and industrial applications. In the present paper, we consider the specific case of the exterior Helmholtz equation which models 2D/3D acoustics and 2D TE/TM electromagnetic waves propagation. Among the most standard accurate computational approaches, let us mention e.g. the high-order finite difference/finite element methods with absorbing/artificial boundary conditions or PMLs [6, 16, 17, 18, 19, 20, 23, 27, 36, 39, 45, 50, 51, 52, 69, 73, 74, 76, 80, 82] to get a bounded computational domain and solved by iterative or hybrid solvers [12, 22, 40, 41, 42, 53], the boundary element approximation of preconditioned iterative integral equation formulations [9, 24, 28, 64] accelerated by fast evaluation algorithms like the Fast Multipole Method [25, 26, 46, 56, 70] or $\mathcal{H}$-matrix algorithms [21, 47, 57], and the infinite element methods [13]. Concerning the asymptotic numerical approaches, the On-Surface Radiation Condition (OSRC) method [1, 2, 3, 4, 5, 10, 14, 58, 62, 63] has proved to be an interesting prediction tool to efficiently compute far field patterns or as a key ingredient in a more accurate standard numerical method, e.g. as a preconditioner in integral equations formulations [7, 8, 9] or as transmitting boundary conditions for optimized Schwarz domain decomposition methods [12, 22, 41, 42]. All these developments are first formulated at the continuous level, and next a numerical approximation scheme (e.g. finite element or boundary element method) is applied to discretize the resulting equations. For scattering problems, it is desirable to go towards accurate numerical discretization schemes to minimize e.g. the pollution/dispersion effects arising in the numerical approximations, while also considering a highly precise representation of the scattering surface.

Among the numerical methods that combine high precision representations of both the geometry and physical solution, Isogeometric analysis (IGA) has proved to be an extremely powerful tool to compute highly accurate PDE solutions in various fields of interest in engineering. Introduced by Hughes *et al.* in 2005 [48], the use of Non-Uniform Rational B-Spline (NURBS) allows to extend the finite element method not only to represent the solution to the physical problem but also the geometry, which bridges the gap between the finite element method and computer aided design (CAD) tools [31, 32, 49, 65, 66, 81]. In particular, NURBS-based IGA was applied successfully in [54] to high-frequency 2D/3D acoustic scattering problems for the volume formulation with low- and high-order absorbing boundary conditions. It was shown that IGA can indeed lead to high precision solutions while reducing notably the pollution/dispersion error that can be met e.g. in finite element methods. Extensions were later reported e.g. in [15, 34, 35, 37, 55, 79] for various improvements. IGA approximation was also applied with success in [72] for the numerical approximation of standard integral equation formulations arising in acoustic scattering, resulting in IGABEM approximations (see also [29, 38, 67, 68, 77, 83]). IGA with infinite element was also proposed very recently [78]. These references show again that IGA has a great potentiality to compute accurate wave fields.

As previously noticed, since the OSRC method is used as a tool for both volume and surface acoustic formulations, and that many recent contributions have shown that IGA is a very interesting discretization technique for both volume and surface formulations, it is natural to analyze the behavior of IGA when approximating the OSRC formulations, which is the first goal of the paper, resulting in the IGA-OSRC method. In addition, in several high frequency methods [11, 43, 44, 59, 60, 61, 75], an ansatz of the solution can be used to partially cancel the high oscillations arising in the unknown wave field, leading therefore to the possibility of reducing greatly the number of degrees of freedom involved in the numerical method, and, as a consequence, of the size of the linear system to resolve. Here, we propose a Phase Reduction (PR) formulation [11, 43] of the OSRC method, called PR-OSRC formulation, using the plane wave approximation as ansatz (but other possible ansatz could be similarly used according to the situation). The PR-OSRC is also next approximated by IGA, leading therefore to the IGA-PR-OSRC method, that is favorably compared with the IGA-OSRC scheme. This opens the possibility to directly implement efficient and accurate OSRC-based formulations that could be used later to improve volume and surface based wave scattering formulations approximated by IGA.

The plan of the paper is the following. Section 2 presents the OSRC and PR-OSRC formulations by considering the Padé-type OSRC developed in [10]. The IGA approximation of both formulations is then explained in Section 3. The simple case of the disk is analyzed in details in Section 4 to understand the different features of the methods. More numerical examples are presented in Section 5 in 2D and Section 6 in 3D. We finally end by a conclusion in Section 7.

2. OSRC and PR-OSRC formulations

2.1. The time-harmonic scattering problem

Let us denote the scatterer by Ω^-, defined as a d-dimensional bounded set of $\mathbb{R}^d$ with boundary $\Gamma := \partial\Omega^-$. We introduce the corresponding exterior domain of propagation $\Omega^+ := \mathbb{R}^d \backslash \overline{\Omega^-}$. We assume that a Dirichlet or a Neumann boundary condition (sound-soft/sound-hard boundary condition) is prescribed on Γ by a function g. Our goal is to compute the time-harmonic wave field u solution to

$$\left\{ \begin{array}{l} \Delta u + k^2 u = 0, \quad \text{in} \quad \Omega^+, \\ u = g \text{ or } \partial_{\mathbf{n}} u_{|\Gamma} = g \text{ on } \Gamma, \\ \lim\limits_{||\mathbf{x}||\to+\infty} ||\mathbf{x}||^{(d-1)/2} (\nabla u \cdot \dfrac{\mathbf{x}}{||\mathbf{x}||} - iku) = 0, \end{array} \right. \tag{1}$$

where Δ is the Laplacian operator, ∇ the gradient operator and $\mathbf{n}$ is the outwardly directed unit normal vector to Ω^-. The wave number k is related to the wavelength λ by the relation: $\lambda := 2\pi/k$. Denoting by $\mathbf{a} \cdot \mathbf{b}$ the hermitian inner-product of two complex-valued vector fields $\mathbf{a}$ and $\mathbf{b}$, then the last equation of system (1) is known as the Sommerfeld's radiation condition at infinity [28, 64], ensuring the uniqueness of the solution to the BVP.

2.2. The OSRC method and its standard formulation

The technique of On-Surface Radiation Conditions (OSRC) for scattering problems consists in writing an approximation Λ^{app} of the exact DtN operator Λ^{ex} defining the exact

nonlocal relation $\partial_{\mathbf{n}} u = \Lambda^{\text{ex}} u$ over the scattering surface Γ. This results in an approximate relation $\psi = \Lambda^{\text{app}} \rho$, with $\psi \approx \partial_{\mathbf{n}} u$ or/and $\rho \approx u$ on Γ. One of the fundamental requirements related to OSRCs is that they are defined explicitly or implicitly by a local operator, i.e. a surface PDE, or a system of surface PDEs on Γ. In the present paper, we illustrate the full methodology by considering the Padé-type OSRC introduced in [10] which has been proved to be accurate, in particular when considering the high-frequency regime corresponding to λ small compared to the characteristic size of Ω^-.

More precisely, the approximation of Λ^{ex} uses the α-rotated Padé's approximation of order N of the square-root OSRC

$$\psi = ik\sqrt{\mathbb{I} + X}\rho, \tag{2}$$

with

$$X = \text{div}_\Gamma(\frac{1}{k_\epsilon^2}\nabla_\Gamma \cdot), \tag{3}$$

leading to the local PDE representation [10]

$$\psi = ik(c_0\rho + \sum_{j=1}^{N} c_j\phi_j), \quad \text{on } \Gamma, \tag{4}$$

with

$$\text{div}_\Gamma(\frac{d_j}{k_\epsilon^2}\nabla_\Gamma\phi_j) + \phi_j = \text{div}_\Gamma(\frac{1}{k_\epsilon^2}\nabla_\Gamma\rho), \quad \text{on } \Gamma. \tag{5}$$

In the above equation, ∇_Γ designates the surface gradient over Γ of a scalar surface field while div_Γ is the divergence of a surface vector field. The identity operator on Γ is denoted by $\mathbb{I}$. The complex wavenumber k_ϵ is such that: $k_\epsilon := k + i\epsilon$, where $\epsilon := 0.4k^{1/3}\mathcal{H}^{2/3}$, with $\mathcal{H}$ the local mean curvature of Γ. For $j = 1 \cdots N$, the complex-valued Padé coefficients of order N are given by

$$c_0 = e^{i\alpha/2}R_N(e^{-i\alpha} - 1), \qquad c_j = \frac{e^{-i\frac{\alpha}{2}}a_j}{(1 + b_j(e^{-i\alpha} - 1))^2}, \qquad d_j = \frac{e^{-i\alpha}b_j}{1 + b_j(e^{-i\alpha} - 1)}, \tag{6}$$

with

$$a_j = \frac{2}{2N+1}\sin^2(\frac{j\pi}{2N+1}), \qquad b_j = \cos^2\left(\frac{j\pi}{2N+1}\right), \tag{7}$$

and the standard real-valued Padé approximation of order N is

$$R_N(z) = 1 + \sum_{j=1}^{N} \frac{a_j z}{1 + b_j z}. \tag{8}$$

The resulting rotating Padé approximation is then given by

$$R_{N,\alpha}(z) = c_0 + \sum_{j=1}^{N} \frac{c_j z}{1 + d_j z}. \tag{9}$$

Let us consider now that we are solving a sound-soft scattering problem. Then, we set $\rho = g = -u^{\text{i}}$ on Γ, where u^{i} is the incident field (usually a plane wave). The OSRC

method with Padé's approximation can be decomposed into two steps. First, we determine the auxiliary surface functions ϕ_j, $j = 1, ..., N$, solutions to the weak variational formulation: find $\phi_j \in H^1(\Gamma)$, such that, $\forall v_j \in H^1(\Gamma)$,

$$-\int_\Gamma \frac{d_j}{k_\epsilon^2}\nabla_\Gamma\phi_j \cdot \nabla_\Gamma v_j d\Gamma + \int_\Gamma \phi_j v_j d\Gamma = \int_\Gamma \frac{1}{k_\epsilon^2}\nabla_\Gamma u^{\mathrm{i}} \cdot \nabla_\Gamma v_j d\Gamma. \tag{10}$$

Next, the normal derivative trace $\partial_{\mathbf{n}} u_{|\Gamma}$ is approximated by ψ based on

$$\psi = ik(-c_0 u^{\mathrm{i}} + \sum_{j=1}^{N} c_j \phi_j), \tag{11}$$

which completes the Cauchy data required to calculate the scattered field. Indeed, we have the exact Helmholtz integral representation formula, for $\mathbf{x} \in \Omega^+$,

$$u(\mathbf{x}) = \int_\Gamma \left[\partial_{\mathbf{n}(\mathbf{y})} G(\mathbf{x},\mathbf{y}) u(\mathbf{y}) - G(\mathbf{x},\mathbf{y})\partial_{\mathbf{n}(\mathbf{y})} u(\mathbf{y})\right] d\Gamma(\mathbf{y}), \tag{12}$$

which allows us to determine the exterior wavefield, where G designates the Green's function given in 2D by

$$G(\mathbf{x},\mathbf{y}) = \frac{i}{4} H_0^{(1)}(k||\mathbf{x}-\mathbf{y}||) \tag{13}$$

and in 3D through

$$G(\mathbf{x},\mathbf{y}) = \frac{e^{ik||\mathbf{x}-\mathbf{y}||}}{4\pi||\mathbf{x}-\mathbf{y}||}. \tag{14}$$

Here, $H_0^{(1)}$ stands for the first-kind Hankel function of order zero. From the approximate OSRC Cauchy data $(\rho, \psi) = (-u^{\mathrm{i}}, \psi)$, we evaluate the scattered field by replacing $(u, \partial_{\mathbf{n}} u_{|\Gamma})$ by its OSRC approximation in (12). Similarly, we can compute the far-field pattern (Radar Cross Section (RCS)) in 2D based on the formula (in decibels (dB))

$$\mathrm{RCS}(\theta) = 10\log_{10}\left(2\pi|a_0(\theta)|^2\right) \quad (\mathrm{dB}), \tag{15}$$

where (r, θ) is the polar coordinate system and $a_0(\theta)$ is the r-independent scattering amplitude [9, 28, 64] given by

$$a_0(\theta) = \frac{e^{\frac{i\pi}{4}}}{\sqrt{8\pi ik}} \int_\Gamma \left(\partial_{\mathbf{n}(\mathbf{y})} u(\mathbf{y}) + ik\boldsymbol{\theta}\cdot\mathbf{n}(\mathbf{y})u(\mathbf{y})\right) e^{-ik\boldsymbol{\theta}\cdot\mathbf{y}} d\Gamma(\mathbf{y}), \tag{16}$$

where $\boldsymbol{\theta} = (\cos(\theta), \sin(\theta))^T$ is the vector of observation in the polar coordinate system. In 3D, one gets the expression

$$\mathrm{RCS}(\theta,\varphi) = 10\log_{10}\left(4\pi|a_0(\theta,\varphi)|^2\right) \quad (\mathrm{db}), \tag{17}$$

where (r, θ, φ) are the spherical coordinates, and $a_0(\theta, \varphi)$ is the scattering amplitude in the (θ, φ)-direction defined by

$$a_0(\theta,\varphi) = \frac{1}{4\pi} \int_\Gamma \left(\partial_{\mathbf{n}(\mathbf{y})} u(\mathbf{y}) + ik\boldsymbol{\theta}\cdot\mathbf{n}(\mathbf{y})u(\mathbf{y})\right) e^{-ik\boldsymbol{\theta}\cdot\mathbf{y}} d\Gamma(\mathbf{y}), \tag{18}$$

setting $\boldsymbol{\theta} := (\cos(\theta)\cos(\phi), \sin(\theta)\cos(\varphi), \sin(\varphi))^T$.

In the case of a Neumann boundary condition (sound-hard acoustic problem), then we have: $\psi = \partial_{\mathbf{n}} u_{|\Gamma} = g = -\partial_{\mathbf{n}} u^{\mathrm{i}}_{|\Gamma}$. Therefore, based on the Padé's OSRC approximation, we have to solve the following coupled system of PDEs: find $\rho \approx u \in H^1(\Gamma)$ such that, $\forall v \in H^1(\Gamma)$,

$$ikc_0 \int_\Gamma \rho v \Gamma + ik \sum_{j=1}^{N} \int_\Gamma c_j \phi_j v \Gamma = -\int_\Gamma \partial_{\mathbf{n}} u^{\mathrm{i}}_{|\Gamma} v d\Gamma, \tag{19}$$

together with: for $1 \leq j \leq N$, find $\phi_j \in H^1(\Gamma)$ such that, $\forall v_j \in H^1(\Gamma)$,

$$\int_\Gamma \frac{1}{k_\epsilon^2} \nabla_\Gamma \rho \cdot \nabla_\Gamma v_j d\Gamma - \int_\Gamma \frac{d_j}{k_\epsilon^2} \nabla_\Gamma \phi_j \cdot \nabla_\Gamma v_j d\Gamma + \int_\Gamma \phi_j v_j d\Gamma = 0. \tag{20}$$

The approximate Cauchy data $(\rho, -\partial_{\mathbf{n}} u^{\mathrm{i}}_{|\Gamma})$ can then be used to evaluate the scattered field, and most particularly the RCS. The extension to other kinds of boundary conditions is direct.

Finally, let us remark that an alternative formulation could be derived based on the following idea. We can formally write a new OSRC equation

$$\sqrt{\mathbb{I} + X}\psi = ik(\mathbb{I} + X)\rho$$

which corresponds to composing the initial square-root OSRC equation (2) on both sides by $\sqrt{\mathbb{I} + X}$. Now, for the Neumann problem, ψ is known, and we solve the equation in two steps, first computing

$$W = \sqrt{\mathbb{I} + X}\psi \tag{21}$$

which is localized thanks to the Padé approximants to get W, and next

$$ik(\mathbb{I} + X)\rho = W, \tag{22}$$

to obtain ρ. This means that for (21) we can easily adapt the Dirichlet code to get the approximation of W. Even if the method is interesting since the first step leads to solving uncoupled equations, this formulation usually provides a less accurate numerical solution and is not considered in the paper.

2.3. Phase Reduction OSRC formulation (PR-OSRC)

We now propose to develop a Phase Reduction OSRC (called PR-OSRC) formulation based on a plane wave approximation approach.

Let us first fix the Dirichlet problem for a plane wave illuminating the obstacle, i.e. $u^{\mathrm{i}}(\mathbf{x}) := e^{i\mathbf{k}^{\mathrm{i}}\cdot\mathbf{x}}$. We set the trace u as: $u(\mathbf{x}) := -e^{i\mathbf{k}^{\mathrm{i}}\cdot\mathbf{x}}$ over Γ, where $\mathbf{k}^{\mathrm{i}} = k\boldsymbol{\theta}^{\mathrm{i}}$ and $\boldsymbol{\theta}^{\mathrm{i}}$ is the incidence vector. More generally, we have

$$\begin{aligned}
\nabla_\Gamma(A(\mathbf{x})e^{i\mathbf{k}^{\mathrm{i}}\cdot\mathbf{x}}) &= \nabla(A(\mathbf{x})e^{i\mathbf{k}^{\mathrm{i}}\cdot\mathbf{x}}) - \mathbf{n}(\mathbf{n}\cdot\nabla(A(\mathbf{x})e^{i\mathbf{k}^{\mathrm{i}}\cdot\mathbf{x}})) \\
&= ((\nabla A + i\mathbf{k}^{\mathrm{i}}A) - \mathbf{n}(\mathbf{n}\cdot(\nabla A + i\mathbf{k}^{\mathrm{i}}A)))e^{i\mathbf{k}^{\mathrm{i}}\cdot\mathbf{x}} \\
&= (\nabla_\Gamma A + i(\mathbf{k}^{\mathrm{i}} - \mathbf{n}(\mathbf{n}\cdot\mathbf{k}^{\mathrm{i}}))A)e^{i\mathbf{k}^{\mathrm{i}}\cdot\mathbf{x}} \\
&= (\nabla_\Gamma A + i\mathbf{k}^{\mathrm{i}}_\Gamma A)e^{i\mathbf{k}^{\mathrm{i}}\cdot\mathbf{x}},
\end{aligned}$$

where the tangential incident wavenumber $\mathbf{k}^{\mathrm{i}}_\Gamma$ is defined by: $\mathbf{k}^{\mathrm{i}}_\Gamma := \mathbf{k}^{\mathrm{i}} - (\mathbf{n}\cdot\mathbf{k}^{\mathrm{i}})\mathbf{n}$. Therefore, writing similar relations for both $\phi_j = A_j e^{i\mathbf{k}^{\mathrm{i}}\cdot\mathbf{x}}$ and $v_j := B_j e^{-i\mathbf{k}^{\mathrm{i}}\cdot\mathbf{x}}$, one gets, for $j = 1, ..., N$, the PR-OSRC formulation of system (10)

$$\begin{aligned}\int_\Gamma -\frac{d_j}{k_\epsilon^2}(\nabla_\Gamma A_j + i\mathbf{k}^{\mathrm{i}}_\Gamma A_j)\cdot(\nabla_\Gamma B_j - i\mathbf{k}^{\mathrm{i}}_\Gamma B_j) + A_j B_j d\Gamma \\ = \int_\Gamma \frac{1}{k_\epsilon^2} i\mathbf{k}^{\mathrm{i}}_\Gamma \cdot (\nabla_\Gamma B_j - i\mathbf{k}^{\mathrm{i}}_\Gamma B_j) d\Gamma,\end{aligned} \tag{23}$$

since $\nabla_\Gamma u^{\mathrm{i}} = i\mathbf{k}^{\mathrm{i}}_\Gamma e^{i\mathbf{k}^{\mathrm{i}}\cdot\mathbf{x}}$. The functions A_j and B_j are supposed to be some complex-valued functions with low frequency oscillations, similarly to the PR method developed for volume formulations in [11, 43]. Expanding the above formulation, we obtain

$$\begin{aligned}\int_\Gamma -\frac{d_j}{k_\epsilon^2}\nabla_\Gamma A_j\cdot\nabla_\Gamma B_j - i\frac{d_j}{k_\epsilon^2}(A_j(\mathbf{k}^{\mathrm{i}}_\Gamma\cdot\nabla_\Gamma B_j) - (\mathbf{k}^{\mathrm{i}}_\Gamma\cdot\nabla_\Gamma A_j)B_j) \\ +(1 - \frac{d_j}{k_\epsilon^2}||\mathbf{k}^{\mathrm{i}}_\Gamma||^2)A_j B_j d\Gamma = \int_\Gamma \frac{1}{k_\epsilon^2} i\mathbf{k}^{\mathrm{i}}_\Gamma\cdot(\nabla_\Gamma B_j - iB_j\mathbf{k}^{\mathrm{i}}_\Gamma)d\Gamma.\end{aligned} \tag{24}$$

Then, in a second step, the normal derivative trace is approximated thanks to the slowly varying amplitude Ψ

$$\partial_{\mathbf{n}} u_{|\Gamma} \approx \psi := \Psi(\mathbf{x}) e^{i\mathbf{k}^{\mathrm{i}}\cdot\mathbf{x}}$$

and

$$\Psi(\mathbf{x}) = ik(-c_0 + \sum_{j=1}^{N} c_j A_j(\mathbf{x})). \tag{25}$$

Once these quantities are obtained, the Cauchy data are approximated by $(u_{|\Gamma}, \partial_{\mathbf{n}} u_{|\Gamma}) \approx (-1, \Psi)e^{i\mathbf{k}^{\mathrm{i}}\cdot\mathbf{x}}$. In the present paper, for the RCS computations, we directly inject the Cauchy data evaluated against the plane wave function in (16) or (18), leading for example to the 2D PR-OSRC approximation of a_0

$$a_0(\theta) \approx a_0^{\mathrm{PR}}(\theta) = \frac{1}{\sqrt{8\pi k}} \int_\Gamma (\Psi(\mathbf{y}) + ik\boldsymbol{\theta}\cdot\mathbf{n}(\mathbf{y}))\, e^{ik(\boldsymbol{\theta}^{\mathrm{i}} - \boldsymbol{\theta})\cdot\mathbf{y}} d\Gamma(\mathbf{y}). \tag{26}$$

Specific methods could also be used, even within the framework of IGA, by considering quadrature rules for approximating highly oscillatory functions or techniques as the ones related to high frequency integral equations [33]. However, we only apply a direct quadrature evaluation in the paper.

Finally, the PR-OSRC method can be extended to the Neumann problem based on the previous formulation (19)-(20). More precisely, setting $\rho(\mathbf{x}) = U(\mathbf{x})e^{i\mathbf{k}^{\mathrm{i}}\cdot\mathbf{x}}$ and with $\partial_{\mathbf{n}} u_{|\Gamma} = -i(\mathbf{k}^{\mathrm{i}}\cdot\mathbf{n})e^{i\mathbf{k}^{\mathrm{i}}\cdot\mathbf{x}}$, by using the same notations as above, one gets from (19)

$$ikc_0 \int_\Gamma UB d\Gamma + ik\sum_{j=1}^{N}\int_\Gamma c_j A_j B d\Gamma = \int_\Gamma i\mathbf{k}^{\mathrm{i}}\cdot\mathbf{n} B d\Gamma, \tag{27}$$

and, for (20), we obtain

$$\int_\Gamma \frac{1}{k_\epsilon^2}\nabla_\Gamma U\cdot\nabla_\Gamma B_j + \frac{i}{k_\epsilon^2}(U(\mathbf{k}_\Gamma^{\mathrm{i}}\cdot\nabla_\Gamma B_j) - (\mathbf{k}_\Gamma^{\mathrm{i}}\cdot\nabla_\Gamma U)B_j) + \frac{||\mathbf{k}_\Gamma^{\mathrm{i}}||^2}{k_\epsilon^2}UB_j d\Gamma$$
$$- \int_\Gamma \frac{d_j}{k_\epsilon^2}\nabla_\Gamma A_j\cdot\nabla_\Gamma B_j + \frac{id_j}{k_\epsilon^2}(A_j(\mathbf{k}_\Gamma^{\mathrm{i}}\cdot\nabla_\Gamma B_j) - (\mathbf{k}_\Gamma^{\mathrm{i}}\cdot\nabla_\Gamma A_j)B_j) \tag{28}$$
$$+\frac{d_j}{k_\epsilon^2}||\mathbf{k}_\Gamma^{\mathrm{i}}||^2 A_jB_j d\Gamma + \int_\Gamma A_jB_j d\Gamma = 0.$$

3. IGA approximation of OSRC formulations

3.1. A brief overview of IGA

In [10], the OSRC formulation is approximated by a linear finite element method. Since the OSRC leads to solving systems of surface PDEs, it appears that developing numerical approximation schemes involving directly the geometry description would perfectly fit. In addition, since we are solving (2D) Helmholtz-type surface problems, it is known that pollution effects could arise in a finite element method, even in 2D.

Here, we prospect the possibility of using directly high-order representations of the surface fields and the geometry considering Isogeometric Finite Element Methods (IGA). It was originally developed to directly adopt the computational domain model generated by Computer Aided Design (CAD) in conventional Finite Element Analysis [31, 32, 49, 65, 66, 81]. To achieve this, the basis functions used to describe the domain geometry were considered to estimate the solution. More specifically, B-Splines and Non Uniform Rational B-Splines (NURBS) were used to describe both the physical domain and the solution in IGA. It was shown that IGA can yield higher accuracy per degree of freedom when compared to conventional FEM. Exact geometry based on both polynomials and conic sections such as circles, spheres, and ellipsoids can be represented even using very coarse meshes. Therefore, this exact geometry representation combined with convenient high order analysis makes IGA a promising tool for the analysis of wave propagation problems. For example, the effects of adopting B-Splines on the pollution error was studied for 2D/3D acoustics. In particular, it was observed [54] that the pollution error can be strongly limited by maintaining the discretization density fixed for basis orders $p \geq 3$, even at very high frequencies. IGA also benefits from attractive refinement possibilities such as k-refinement which has no equivalent in conventional FEM. Furthermore, r-refinement for IGA was developed to increase the density of control points where curvature based monitor functions are maximum [84].

In IGA, the parametric definition of the B-Splines/NURBS basis function is directly adopted to discretize a 3D curve. A knot vector is defined as a set of non-decreasing parametric coordinates $\boldsymbol{\xi} = \{\xi_1, \xi_2, ..., \xi_{(n+p+1)}\}, \xi_i \leq \xi_{i+1}$, where ξ_i is the i^{th} knot and i is the knot index, $i = 1, 2, \cdots, n+p+1$, where p is the polynomial order and n is the number of basis functions. The mapping of a non-zero knot span in parametric space to physical space is defined as an element. When a knot ξ_i is repeated k times in the knot vector, its *multiplicity* is k_i and the B-Spline exhibit C^{p-k} continuity in the corresponding physical point. Usually, *open knot vectors* are used in IGA where the first and the last knot values appear $p+1$ times, in other words, first and last knots have $k = p+1$ multiplicity which results in C^0 continuity at the surface patch boundaries or curve end points. This also provides Krönecker delta property at the end points which does not hold for the interior points.

The Cox-de Boor recursion formula is used to define a B-Spline recursively by starting with the zeroth order ($p = 0$) basis function:

$$\text{for } p = 0,\ N_i^p(\xi) = \begin{cases} 1 & \xi_i \le \xi \le \xi_{i+1}, \\ 0 & \text{otherwise}, \end{cases} \tag{29}$$

$$\text{for } p = 1, 2, 3, \cdots \quad N_i^p(\xi) = \frac{\xi - \xi_i}{\xi_{i+p} - \xi_i} N_i^{p-1}(\xi) + \frac{\xi_{i+p+1} - \xi}{\xi_{i+p+1} - \xi_{i+1}} N_{i+1}^{p-1}(\xi), \tag{30}$$

where $0/0$ is defined to be zero. The first-order B-Spline functions are identical to their Lagrangian (FEM) counterparts. B-Splines also provide the partition of unity property, $\sum_{i=0}^{n} N_{i,p}(\xi) = 1$. The number of required shape functions for order p analysis is $p + 1$; $N_{i,p}(\xi) \neq 0$ only when $\xi \in [\xi_i, \xi_{i+p+1}]$. We define

$$R_i^p(\xi) = \frac{N_i^p(\xi) w_i}{W(\xi)} = \frac{N_i^p(\xi) w_i}{\sum_{i=1}^{n} N_i^p(\xi) w_i}, \tag{31}$$

where $\{N_i^p\}_{i=1}^n$ is a set of B-Splines basis functions and $\{w_i\}_{i=1}^n$ is a set of positive NURBS weights. For equal weights, NURBS basis functions reduce to their B-Splines counterparts, $R_i^p = N_i^p$, and the corresponding curve becomes a non-rational polynomial again. Hence, B-Splines are a subset of NURBS. Multivariate NURBS basis functions are generated as the tensor product of univariate basis:

$$R_{i,j}^{p,q}(\xi, \eta) = \frac{N_i^p(\xi) M_{j,q}(\eta) w_{i,j}}{\sum_{i=1}^{n} \sum_{j=1}^{m} N_i^p(\xi) M_{j,q}(\eta) w_{i,j}}, \tag{32}$$

where $N_i^p(\xi)$, and $M_j^q(\eta)$ are B-Splines basis functions of order p, and q respectively. NURBS curves and surfaces are defined as a linear combination of these basis functions and the corresponding control points denoted with $\mathbf{B}$, leading to

$$\mathbf{C}(\xi) = \sum_{i=1}^{n} R_i^p(\xi) \mathbf{B}_i, \quad \mathbf{S}(\xi, \eta) = \sum_{i=1}^{n} \sum_{j=1}^{m} R_{i,j}^{p,q}(\xi, \eta) \mathbf{B}_{i,j}. \tag{33}$$

For completeness, we recommend the review papers [65, 66] for the reader interested in IGA.

3.2. Computation of geometrical features in IGA for OSRC

Benefiting from smoothness of the functions in IGA, we can readily calculate the mean curvature $\mathcal{H}$ (and possibly other geometrical quantities) at each integration point on the surface of the scatterer which is required to calculate the complex wave number $k_\epsilon = k + i\epsilon$ involved in the OSRC definition, with $\epsilon := 0.4 k^{1/3} \mathcal{H}^{2/3}$. It is known that

$$\mathcal{H} = \frac{||\mathbf{C}_{,\xi} \times \mathbf{C}_{,\xi\xi}||}{||\mathbf{C}_{,\xi}||^3} = \frac{x_{,\xi}\, y_{,\xi\xi} - y_{,\xi}\, x_{,\xi\xi}}{(x_{,\xi}^2 + y_{,\xi}^2)^{3/2}}, \tag{34}$$

where $x_{,\xi}$ and $y_{,\xi}$ are the first-order derivatives of the physical map with respect to ξ, while $x_{,\xi\xi}$ and $y_{,\xi\xi}$ are the second-order derivatives. The curvature at a physical point on the surface

(x, y) can be characterized through principal curvatures and curvature directions which can be obtained respectively as the eigenvalues and eigenvectors of the following matrix:

$$\mathbf{A} = -\mathbf{T}_c \mathbf{T}_m^{-1}, \tag{35}$$

where $\mathbf{T}_c$ and $\mathbf{T}_m$ are the metric and curvature tensors of the surface, respectively [71], given by

$$\mathbf{T}_m = \begin{bmatrix} E & F \\ F & G \end{bmatrix} = \begin{bmatrix} \mathbf{C}_{,\xi} \cdot \mathbf{C}_{,\xi} & \mathbf{C}_{,\xi} \cdot \mathbf{C}_{,\eta} \\ \mathbf{C}_{,\eta} \cdot \mathbf{C}_{,\xi} & \mathbf{C}_{,\eta} \cdot \mathbf{C}_{,\eta} \end{bmatrix} \tag{36}$$

and

$$\mathbf{T}_c = \begin{bmatrix} e & f \\ f & g \end{bmatrix} = \begin{bmatrix} \mathbf{n} \cdot \mathbf{C}_{,\xi\xi} & \mathbf{n} \cdot \mathbf{C}_{,\xi\eta} \\ \mathbf{n} \cdot \mathbf{C}_{,\eta\xi} & \mathbf{n} \cdot \mathbf{C}_{,\eta\eta} \end{bmatrix}, \tag{37}$$

where $\mathbf{n}$ is the unit normal vector to the surface

$$\mathbf{n} = \frac{\mathbf{C}_{,\xi} \times \mathbf{C}_{,\eta}}{||\mathbf{C}_{,\xi} \times \mathbf{C}_{,\eta}||}. \tag{38}$$

Then, the principal curvatures $\mathcal{H}_{1,2}$ (and $\mathcal{H} = (\mathcal{H}_1 + \mathcal{H}_2)/2$) are calculated by

$$\mathcal{H}_{1,2} = \frac{-B \pm \sqrt{B^2 - 4AC}}{2A}, \tag{39}$$

where

$$A = \det(\mathbf{T}_m), \quad B = 2Ff - Ge - Eg, \quad C = \det(\mathbf{T}_c). \tag{40}$$

The calculated curvature can be the basis of r-refinement which reduces the error by moving the degrees of freedom [71, 84].

3.3. IGA approximation of the OSRC and PR-OSRC formulations

When compared to a conventional finite element analysis, IGA uses basis functions characterized by a larger support but providing an improved accuracy, for a given approximation order p. In practice, most particularly here in 2D for the OSRC method, this leads to a moderate higher computational cost in the matrix assembly process than the finite element method but for a much better precision. In the following, we denote by n_λ the number of degrees of freedom per wavelength λ involved in the IGA approximation process. The total number of functions overlapping the support of a particular shape function is $2p + 1$, which is similar to that of the conventional finite element method, resulting in the same matrix bandwidth. For 3D acoustics, since we are solving two-dimensional complex-valued Helmholtz-type problems for the OSRC and PR-OSRC formulations with IGA, all the resulting sparse linear systems can be efficiently solved by a LU factorization at a reasonable cost, depending on the matrix size. During the numerical examples reported in the next sections, we show that the PR-OSRC formulation combined with IGA leads to small size sparse linear systems to resolve, while maintaining the accuracy of the OSRC approach.

4. Numerical example: two-dimensional scattering by a disk

4.1. Padé parameters for IGA-OSRC

Let us start by considering the scattering problem by the sound-soft circular cylinder C_{r_0} of radius r_0 (Dirichlet boundary condition), centered at the origin. Then, in this case, for an incident plane wave with zero incidence, we can analytically compute the *reference* normal derivative trace over the surface $\Gamma = C_{r_0}$ as

$$\partial_r u^{\text{ex}}(r_0, \theta) = -k \sum_{n=0}^{+\infty} \epsilon_n i^n \frac{J_n(kr_0)}{H_n^{(1)}(kr_0)} H_n^{(1)'}(kr_0) \cos(n\theta), \tag{41}$$

where ϵ_n is the Neumann function, which is equal to 1 for $n = 0$ and 2 otherwise, and $\theta \in [0; 2\pi]$. The Bessel function of order n is J_n while $H_n^{(1)}$ denotes the first-kind n-th order Hankel function. When using the Padé approximation $R_{N,\alpha}(z)$ of order N and angle α, given by (9), we have the following form of the analytical solution

$$\psi^{\text{Pade}}(r_0, \theta) = -ik \sum_{n=0}^{\infty} \epsilon_n i^n R_{N,\alpha}(-\frac{n^2}{k_\epsilon^2 r_0^2}) J_n(kr_0) \cos(n\theta), \tag{42}$$

with $\epsilon := 0.4k^{1/3} r_0^{-2/3}$. Similarly, for the Neumann boundary condition (sound-hard scatterer), we obtain the analytical form of the OSRC solution for the Padé approximation

$$\rho^{\text{Pade}}(r_0, \theta) = -i \sum_{n=0}^{\infty} \epsilon_n i^n \frac{1}{R_{N,\alpha}(-\frac{n^2}{k_\epsilon^2 r_0^2})} J_n'(kr_0) \cos(n\theta). \tag{43}$$

Let us start by analyzing the optimal values for the Padé order N and rotating angle α for minimizing the relative $L^2(\Gamma)$-error for the IGA solution, with order p and density of degrees of freedom per wavelength n_λ, for a given wave number k. The objective function of this optimization problem is defined as the relative error between the numerical IGA approximation of the Padé OSRC-based normal derivative trace ψ in (4) and the exact reference normal derivative trace $\partial_r u^{\text{ex}}$ given by (41), i.e.

$$\epsilon_{k,p}(N, \alpha) = \frac{||\psi - \partial_r u^{\text{ex}}||_{0,\Gamma}}{||\partial_r u^{\text{ex}}||_{0,\Gamma}}, \tag{44}$$

where $||f||_{0,\Gamma}$ is the $L^2(\Gamma)$-norm of a function f defined over Γ. The minimum of the objective function $\epsilon_{k,p}(N, \alpha)$ is computed by the Differential Evolution algorithm which is known for its speed and ability to find the global solution. Let us remark here that the imposition of the non-homogeneous Dirichlet boundary condition is not straightforward in IGA due to lack of Krönecker delta property. More precisely, when using an open knot vector only the end points satisfy the Krönecker delta property and therefore the value of the boundary condition at these points can be directly applied by setting the control variable equal to the prescribed value. However, this direct imposition is not possible for intermediate control variables where additional treatments become necessary similarly to those common in meshless methods. Usual methods include e.g. Transformation method, Nitsche's method, least squares minimization approach, Lagrange multiplier, penalty and the augmented Lagrangian

methods. In this study, we force the non-homogeneous boundary condition by using the L^2-projection method as described in [30]. The optimal values of the design variables found by the approach (for an error of about $10^{-2.2}$) are listed in Table 1 according to k, for $n_\lambda = 5$ (and $p = 5$). In addition, the relative error $\epsilon_{k,p}(N, \alpha)$ (in $\log_{10}$ scale) with Padé order N and rotation angle α for $k = 50$, and $p = 1, \cdots, 4$ (and $n_\lambda = 5$) are plotted in Fig. 1. It was observed that higher Padé orders N are required for higher frequencies and/or discretization densities n_λ and that, interestingly, the optimum Padé angles α found are decreasing with increased frequency. We also see that the optimal values do not depend on p, which is very interesting in practice for IGA. In [10], it was shown that $\theta = \pi/4$ is a relatively fair choice whatever is N. Figures 1 show that this indeed seems to be again a reasonable global choice in the context of IGA-OSRC, most particularly when $p \geq 2$.

k	10	20	30	40	50	60	100	200	500
N	1	2	2	2	2	3	3	4	5
α	0.677	0.7903	0.6919	0.6148	0.5353	0.7521	0.6117	0.6134	0.398

Table 1: Optimal values of the complex Padé approximation parameters (N, α) vs k ($n_\lambda = 5$).

4.2. Accuracy of IGA-OSRC and IGA-PR-OSRC

We consider now the IGA-OSRC and IGA-PR-OSRC approximations for comparison. Since IGA-PR-OSRC is another formulation of IGA-OSRC involving oscillating functions, we consider the same Padé parameters for both formulations. To illustrate this claim, we report on Figure 2 the behavior of the error thanks to n_λ and N for both formulations, and $k = 40$, $p = 2$ and $\alpha = 0.62$. We can indeed see that the error is similar according to N (but of course for different values of n_λ).

The IGA-OSRC numerical results on the normal derivative trace and RCS for the sound-soft acoustic problem for $k = 40$, $p = 2$, $N = 2$, $\alpha = 0.62$ and $n_\lambda = 5$ (corresponding to 2×197 Degrees of Freedom (DOF)) are reported on Fig. 3. They are compared with the exact reference solution given by expression (41), leading to an error $\epsilon_{k,p}(N, \alpha) = 4.3 \times 10^{-3}$. We can decrease a little bit the number of DOF (nDOF) for $n_\lambda = 4$ by increasing the order p of IGA (see Fig. 4). Then one gets nDOF$= 2 \times 157$ for $p = 5$ and $\epsilon_{k,p}(N, \alpha) = 4.5 \times 10^{-3}$. If we keep on decreasing n_λ from 4 to 3, we start to observe some errors in the computation of the normal derivative trace as seen on Figure 5 for nDOF$= 2 \times 117$ in IGA-OSRC increasing then the error to $\epsilon_{k,p}(N, \alpha) = 2.5 \times 10^{-2}$. However, the RCS is still accurate on Figure 5, which is probably due to the fact that averaging arises in the computation of the integral definition of the scattering amplitude (see Eq. (16)). This example shows that increasing the order p in IGA-OSRC improves the accuracy and allows to have less DOFs. Nevertheless, it is limited by n_λ to correctly represent the oscillations of the surface field.

When using IGA-PR-OSRC, the reduction in nDOF is clearly improved. The IGA-PR-OSRC results for $k = 40$, $p = 2$ and $n_\lambda = 0.8$ (corresponding to 2×29 DOFs) are reported in Fig. 6a. We observe that both the IGA-OSRC (for $n_\lambda = 5$) and IGA-PR-OSRC (with $n_\lambda = 0.8$) formulations lead to solutions that superpose the plot of the exact reference solution, with a similar relative error of 4.3×10^{-3}. In addition, when increasing p, we can

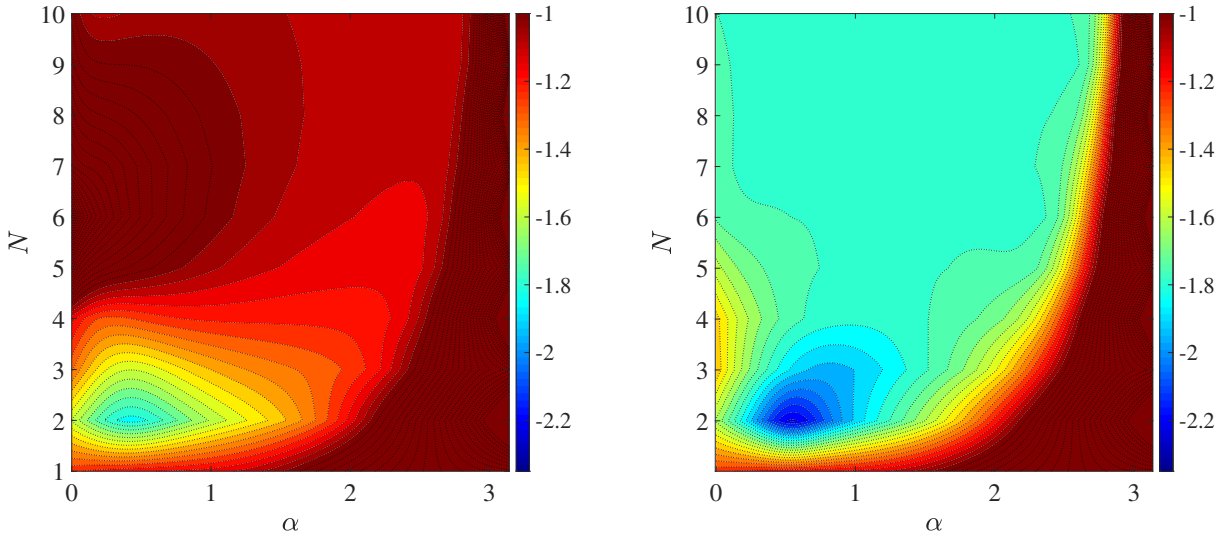

(a) IGA basis order $p = 1$

(b) IGA basis order $p = 2$

(c) IGA basis order $p = 3$

(d) IGA basis order $p = 4$

Figure 1: Dirichlet problem, IGA-OSRC: relative error $\epsilon_{k,p}(N, \alpha)$ (in $\log_{10}$-scale) with Padé order N and rotation angle α for $k = 50$, and $p = 1, \cdots, 4$ in IGA.

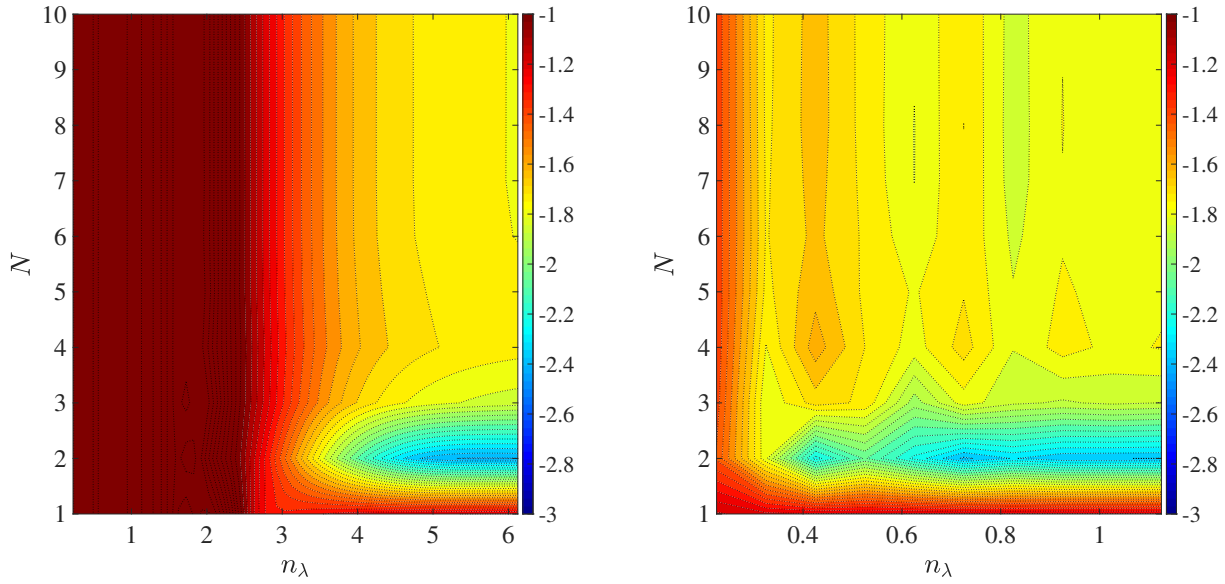

(a) IGA-OSRC (b) IGA-PR-OSRC

Figure 2: Dirichlet problem: evolution of relative error $\epsilon_{k,p}(N, n_\lambda)$ (in $\log_{10}$-scale) with Padé order N and discretization density n_λ for $k = 40$, and $p = 2$, and $\alpha = 0.62$ in (a) IGA-OSRC and (b) IGA-PR-OSRC.

decrease n_λ to 0.6 for nDOF$= 2 \times 21$, which is very low (see Fig. 6b). We observe some small amplitude errors in the normal derivative trace ($\epsilon_{k,p}(N, \alpha) = 4.9 \times 10^{-3}$) but obtain an accurate RCS. These comments extend to other wave numbers k, showing that IGA-PR-OSRC allows to clearly go to only a few DOFs for solving the OSRC formulation, reducing then the computational costs and memory requirements.

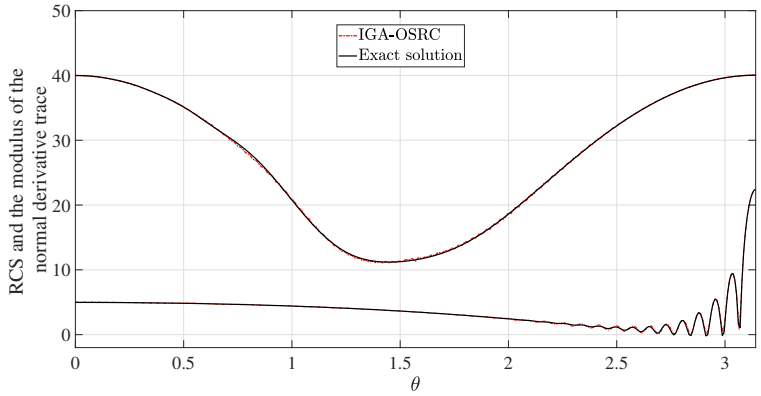

Figure 3: Dirichlet problem: RCS (dB) and amplitude of the normal derivative trace calculated using IGA-OSRC for $k = 40$, $p = 2$, $n_\lambda = 5$ and nDOF $= 2 \times 197$.

To further illustrate this claim for the Dirichlet problem, we report on Figures 7 the convergence curves for the error

$$\epsilon^{\text{Pade}}_{k,p,n_\lambda}(N, \alpha) = \frac{||\psi - \psi^{\text{Pade}}||_{0,\Gamma}}{||\psi^{\text{Pade}}||_{0,\Gamma}} \tag{45}$$

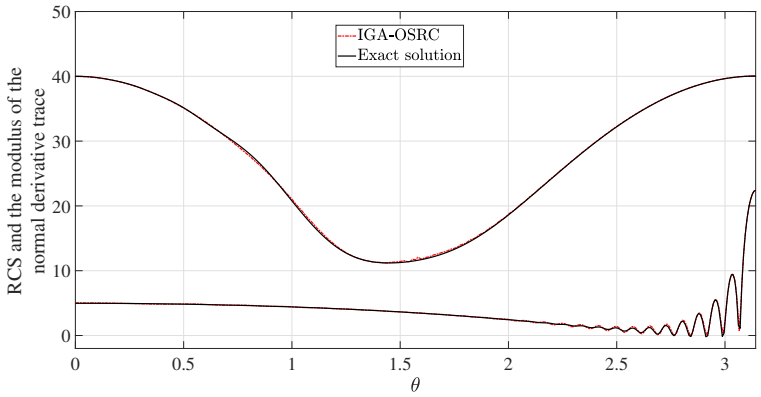

Figure 4: Dirichlet problem: RCS (dB) and amplitude of the normal derivative trace calculated using IGA-OSRC for $k = 40$, $p = 5$, $n_\lambda = 4$ and nDOF $= 2 \times 157$.

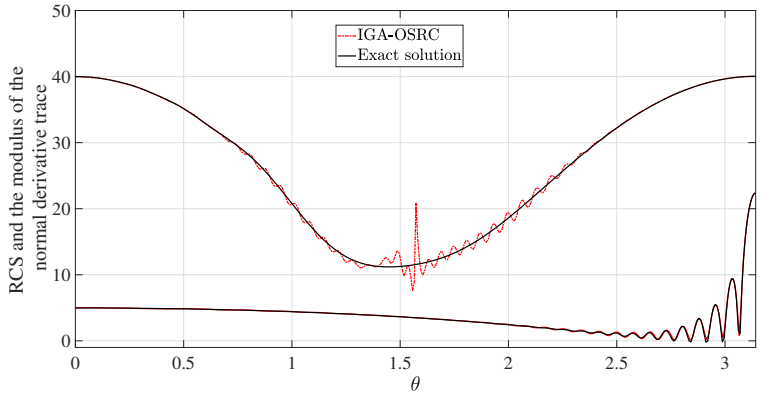

Figure 5: Dirichlet problem: RCS (dB) and amplitude of the normal derivative trace calculated using IGA-OSRC for $k = 40$, $p = 5$, $n_\lambda = 3$ and nDOF $= 2 \times 117$.

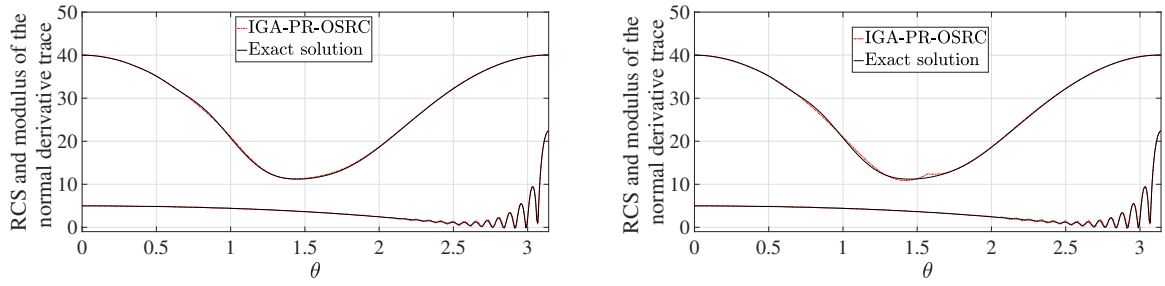

(a) $p = 2$, $n_\lambda = 0.8$ and nDOF $= 2 \times 29$

(b) $p = 5$, $n_\lambda = 0.6$ and nDOF $= 2 \times 21$

Figure 6: Dirichlet problem ($k = 40$) and IGA-PR-OSRC: RCS (dB) and amplitude of the normal derivative trace.

vs the discretization density n_λ (and nDOF), for IGA-OSRC and IGA-PR-OSRC and various orders p. We fix $N = 2$ and $\alpha = 0.54$, for $k = 50$. We directly see that increasing the IGA order p increases the accuracy and leads to smaller nDOF. In addition, the IGA-PR-OSRC requires less DOF for a given accuracy considering a small value of n_λ. IGA-PR-OSRC is

therefore considered as a suitable formulation for the OSRC solution with Dirichlet boundary condition.

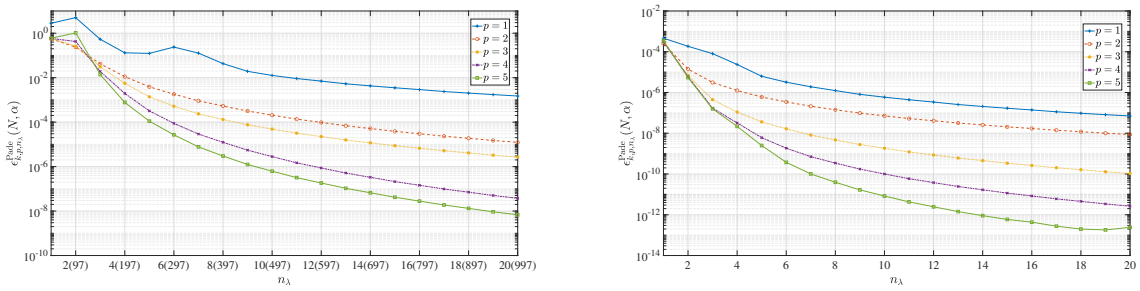

(a) IGA-OSRC

(b) IGA-PR-OSRC

Figure 7: Dirichlet problem ($k = 50$): evolution of the relative error $\epsilon^{\text{Pade}}_{k,p,n_\lambda}(N,\alpha)$ vs. n_λ(nDOF) for various values of p.

Now, let us fix the Neumann problem (sound-hard scattering). We define the error $\epsilon_{k,p}(N,\alpha)$ by

$$\epsilon_{k,p}(N,\alpha) = \frac{||\rho - u^{\text{ex}}||_{0,\Gamma}}{||u^{\text{ex}}||_{0,\Gamma}}, \tag{46}$$

with

$$u^{\text{ex}}(r_0,\theta) = -\sum_{n=0}^{+\infty} \epsilon_n i^n \frac{J_n'(kr_0)}{H_n'^{(1)}(kr_0)} H_n^{(1)}(kr_0)\cos(n\theta). \tag{47}$$

We also introduce the error

$$\epsilon^{\text{Pade}}_{k,p,n_\lambda}(N,\alpha) = \frac{||\rho - \rho^{\text{Pade}}||_{0,\Gamma}}{||\rho^{\text{Pade}}||_{0,\Gamma}}.$$

The trace and RCS for the IGA-PR-OSRC solution of the sound-hard acoustic problem for $k = 40$, $p = 5$, $N = 3$, $\alpha = 0.62$ and $n_\lambda = 3$ (corresponding to 3×117 DOF) are reported on Fig. 8. They are compared with the exact reference solution given by expression (47), leading to an error $\epsilon_{k,p}(N,\alpha) = 1.37 \times 10^{-2}$. The IGA-PR-OSRC is always more accurate than IGA-OSRC for a given density of degrees of freedom, but the difference is more moderate than for the Dirichlet problem. This can be understood from the plane wave ansatz which is probably more adapted to the Dirichlet than Neumann problem. Other choices of ansatz can be considered, even for more complicate objects, since the IGA-PR-OSRC approach can be adapted to other phase functions. To illustrate the behavior of IGA-PR-OSRC vs IGA-OSRC, we plot the convergence curves $\epsilon^{\text{Pade}}_{k,p,n_\lambda}(N,\alpha)$ for various values of the order p by refining. We indeed see that IGA-PR-OSRC remains better than IGA-OSRC. Here, we fixed $N = 2$ and $\alpha = 0.54$.

5. Scattering by a submarine-like shaped scatterer

Now, let us consider a more complicate scatterer which models a simplified submarine-like obstacle. To analyze the IGA-PR-OSRC approach, we decompose the analysis into three intermediate geometrical cases: i) the main convex part of the toy submarine (see Fig. 10a),

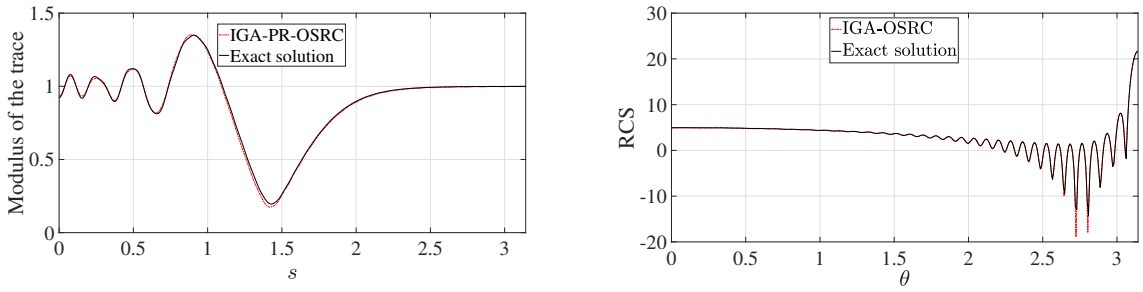

(a) Amplitude of the trace

(b) RCS (dB)

Figure 8: Neumann problem: numerical solution using IGA-PR-OSRC for $k = 40$, $p = 5$, $n_\lambda = 3$, $\epsilon_{k,p}(N, \alpha) = 1.37 \times 10^{-2}$.

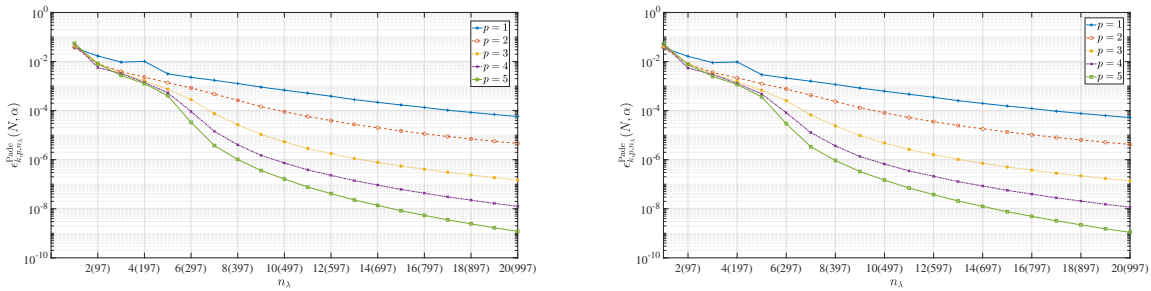

(a) IGA-OSRC

(b) IGA-PR-OSRC

Figure 9: Neumann problem ($k = 50$): evolution of the relative error $\epsilon^{\text{Pade}}_{k,p,n_\lambda}(N, \alpha)$ vs. n_λ(nDOF) for various values of p.

ii) the convex part plus the stabilizer fins (see Figure 11a), and then iii) the full scatterer by adding a tower (Figure 12a). We consider an incident plane wave with $k = 30$ and incidence $\boldsymbol{\theta}^{\text{i}} := (\cos(\theta^{\text{i}}), \sin(\theta^{\text{i}}))$, setting $\theta^{\text{i}} = 5\pi/6$. In all what follows, the reference solution is accurately computed thanks to the IGA-FEABC method developed in [55], which consists in a volume variational formulation with high-order ABC and IGA discretization.

Let us start with the convex part of the submarine (Fig. 10a). The reference solution in the domain is plotted on Figure 10b. For IGA-PR-OSRC, we consider $N = 2$ Padé functions for the rotating angle $\alpha = 0.69$. IGA is based on a mesh involving 74 points. Let us remark that this is needed to describe correctly the geometry of the submarine. The IGA-PR-OSRC solution (RCS and normal derivative trace) is computed by using basis order $p = 2$ and only nDOF $= 2 \times 74$ degrees of freedom. We report the RCS on Figure 10c for both IGA-PR-OSRC and IGA-FEABC. We see that IGA-PR-OSRC leads to an accurate solution at low computational cost. For completeness, we also plot on Figure 10d the amplitude of the approximate normal derivative traces with respect to the curvilinear abscissa s over Γ (s starts at $(1, 0)$ and is counterclockwise directed). We again see that the surface field is well reproduced even if a discrepancy arises at point $(1, 0)$.

We now modify the shape by adding the stabilizer fins as shown in Fig. 11a and obtain the reference solution again by using IGA-FEABC as shown in Fig. 11b. IGA-PR-OSRC is based on the basis of order $p = 2$, for $N = 2$ Padé functions and $\alpha = 0.69$, leading to nDOF $= 2 \times 106$. The corresponding RCS are plotted for IGA-PR-OSRC and IGA-

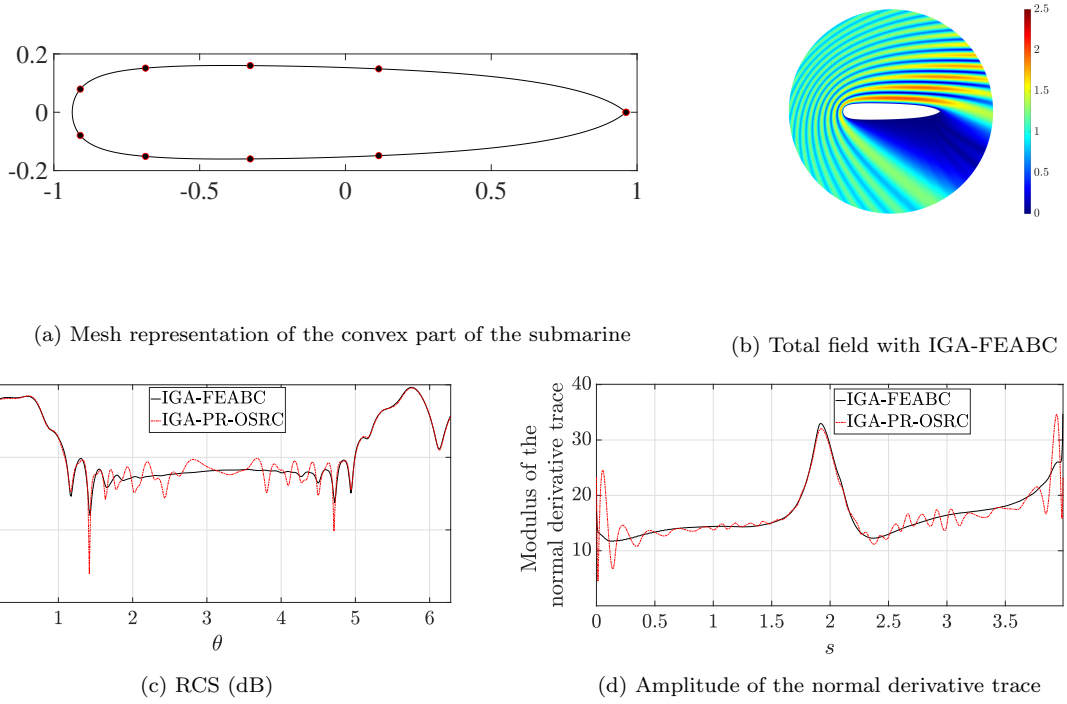

(a) Mesh representation of the convex part of the submarine

(b) Total field with IGA-FEABC

(c) RCS (dB)

(d) Amplitude of the normal derivative trace

Figure 10: Scattering by the convex part of a simplified sound-soft submarine. The plane wave is characterized by $k = 30$ and $\theta^{\mathrm{i}} = 5\pi/6$. IGA-PR-OSRC uses basis functions of order $p = 2$ and considers nDOF $= 2 \times 74$.

FEABC in Fig. 11c. We observe again a good agreement between the solutions, even if the OSRC approach deteriorates due to the presence of a locally concave part. Nevertheless, this difficulty is inherent to the OSRC and not the numerical scheme itself. Future works will address this problem based on computational procedures. Finally, we report on Figure 11d the magnitude of the approximate normal derivatives and see that the field is correctly reproduced even if some errors are locally visible near the stabilizer.

To end this analysis for the sound-soft case, we consider the full submarine-like shaped obstacle (see Fig. 12a). The total field is represented in Fig. 12b. We observe a more complicate pattern since waves can be multiply scattered, most particularly by the tower. On Figure 12c, we see that this clearly impacts the accuracy of the far-field pattern computation by IGA-PR-OSRC, where $N = 2$, $\alpha = 0.69$, $p = 5$, and nDOF $= 2 \times 78$. This is indeed related to the local error loss on the surface fields based on the OSRC, as seen on Figure 12d. This difficulty needs to be solved to lead to fully useful numerical methods related to the OSRC approximation. In addition, increasing p allows for this situation to also maintain a very low number of unknowns to nDOF $= 2 \times 78$. Let us finally remark that using IGA-OSRC would also require much more points than IGA-PR-OSRC.

Let us now focus on the sound-hard toy submarine. First, we solve with IGA-PR-OSRC the scattering problem by the convex part of the submarine. As noticed for the circular cylinder case, we need a finer discretization because the plane wave ansatz is probably less adapted to the Neumann problem and should be improved. We report on Figure 13 both the RCS (left) and the amplitude of the approximate trace (right). To this end, we use $p = 2$

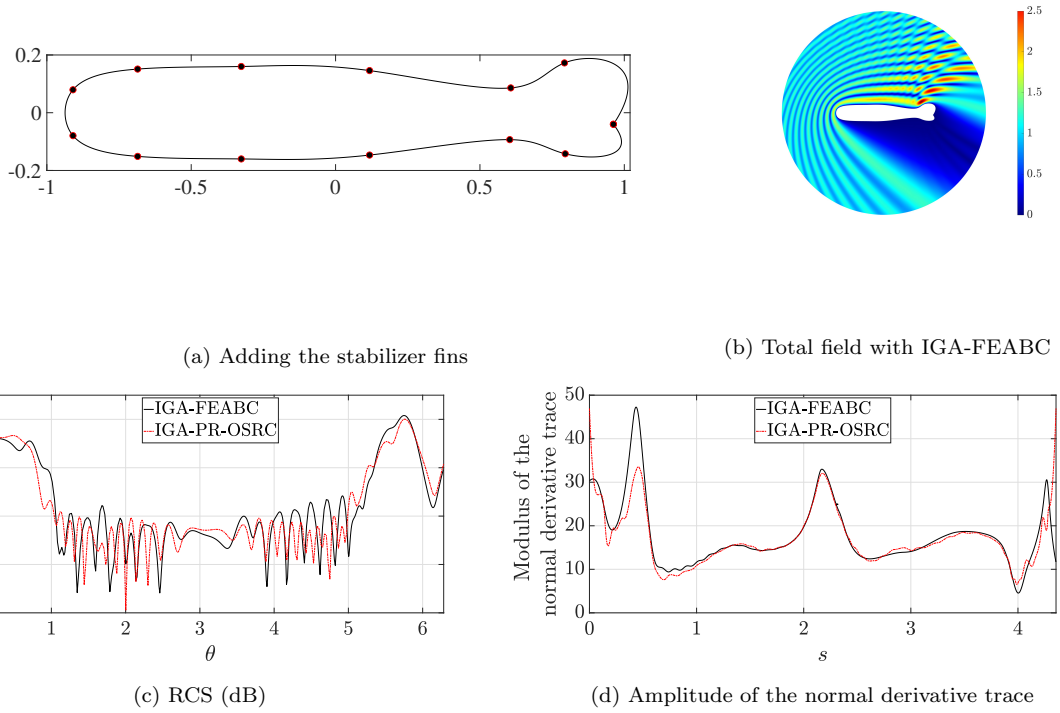

(a) Adding the stabilizer fins

(b) Total field with IGA-FEABC

(c) RCS (dB)

(d) Amplitude of the normal derivative trace

Figure 11: Adding the stabilizer to the convex part of the sound-soft submarine. The plane wave is characterized by $k = 30$ and $\theta^{\mathrm{i}} = 5\pi/6$. IGA-PR-OSRC uses basis functions of order $p = 2$ and considers nDOF $= 2 \times 106$.

for IGA, leading to nDOF $= 2 \times 272$, since again $N = 2$ and $\alpha = 0.69$ are used for the Padé approximation. We can observe that the two quantities are relatively accurate compared with the IGA-FEABC reference solution. Let us also remark that nDOF could also be smaller by keeping a relatively correct solution, in particular when the OSRC quality deteriorates as seen on the two next examples. We report on Figure 14 the same situation but with the stabilizer fins. Here, we use $p = 2$ leading to nDOF $= 2 \times 114$, for the same Padé parameters. We see that we already capture the OSRC accuracy even at this discretization level. To end, we consider the full toy submarine on Figure 15. IGA is based on the basis functions of order $p = 2$, then leading to nDOF $= 2 \times 83$, with the same Padé parameters. Even if clearly some accuracy is lost because of the limits of the OSRC for non convex obstacles, we obtain a good approximation of the RCS at a very low computational cost.

6. Three-dimensional scattering

For completeness, we end by reporting a few computations for three-dimensional problems. Let us start with the scattering problem by the unit sphere. A multi-patch model was developed for both IGA and IGA-PR-OSRC as shown in Figures 16a-16b. The dimension reduction offered by IGA-PR-OSRC is expected to considerably reduce the difficulties encountered when meshing the space around the scatterer in FEM and IGA, avoiding then the solution of a large size linear system. For IGA-FEABC, we use the method introduced

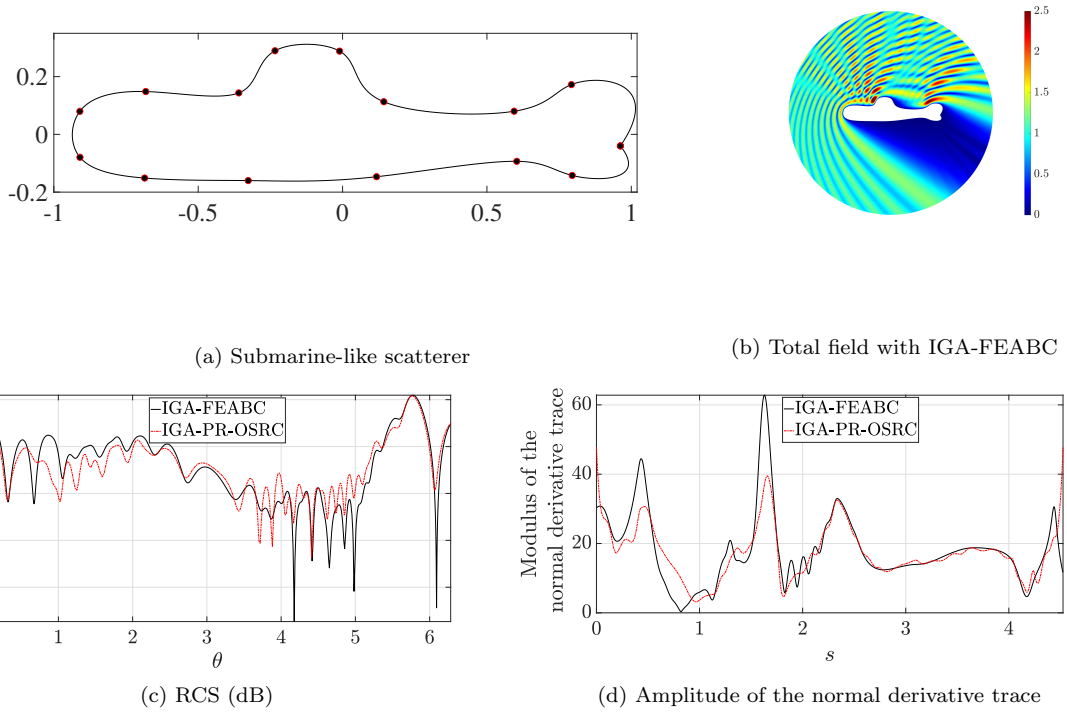

(a) Submarine-like scatterer

(b) Total field with IGA-FEABC

(c) RCS (dB)

(d) Amplitude of the normal derivative trace

Figure 12: Full sound-soft submarine-like shaped scatterer. The plane wave is characterized by $k = 30$ and $\theta^{\mathrm{i}} = 5\pi/6$. IGA-PR-OSRC uses basis functions of order $p = 5$ and considers nDOF $= 2 \times 78$.

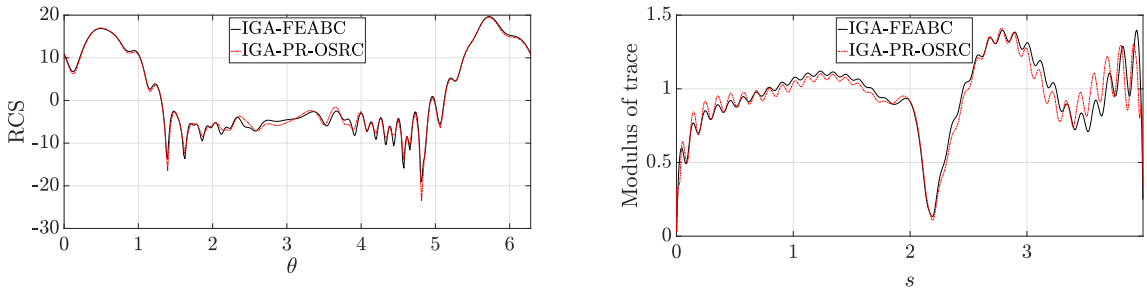

(a) RCS (dB)

(b) Amplitude of the trace

Figure 13: Scattering by the convex part of a simplified sound-hard submarine. The plane wave is characterized by $k = 30$ and $\theta^{\mathrm{i}} = 5\pi/6$. IGA-PR-OSRC uses basis functions of order $p = 2$ and considers nDOF $= 2 \times 272$.

in [37] based on the Wilcox's far-field expansion which serves as a reference computational method for general shapes. The ABC is set on an outer spherical surface of radius 2. For the spherical case, we can alternatively use the exact Mie series expansion ("Exact solution") for comparison.

We first consider the scattering of a plane wave with vector wavenumber $\mathbf{k}^{\mathrm{i}} = k(1, 0, 0)^T$, for $k = 20$ and $k = 40$, by the sound-soft sphere. The modulus of the normal derivative trace over the unit sphere computed by using IGA-PR-OSRC is shown in Fig. 17a for $k = 40$

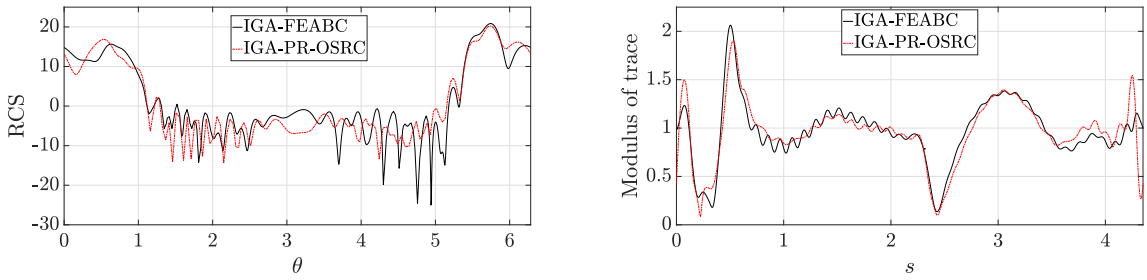

(a) RCS (dB)

(b) Amplitude of the trace

Figure 14: Adding the stabilizer to the convex part of the sound-hard submarine. The plane wave is characterized by $k = 30$ and $\theta^{\mathrm{i}} = 5\pi/6$. IGA-PR-OSRC uses basis functions of order $p = 2$ and considers nDOF $= 2 \times 114$.

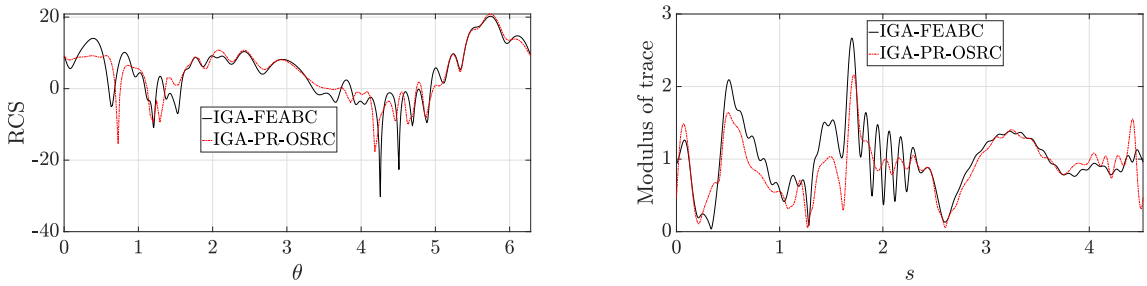

(a) RCS (dB)

(b) Amplitude of the trace

Figure 15: Full sound-hard submarine-like shaped scatterer. The plane wave is characterized by $k = 30$ and $\theta^{\mathrm{i}} = 5\pi/6$. IGA-PR-OSRC uses basis functions of order $p = 5$ and considers nDOF $= 2 \times 83$.

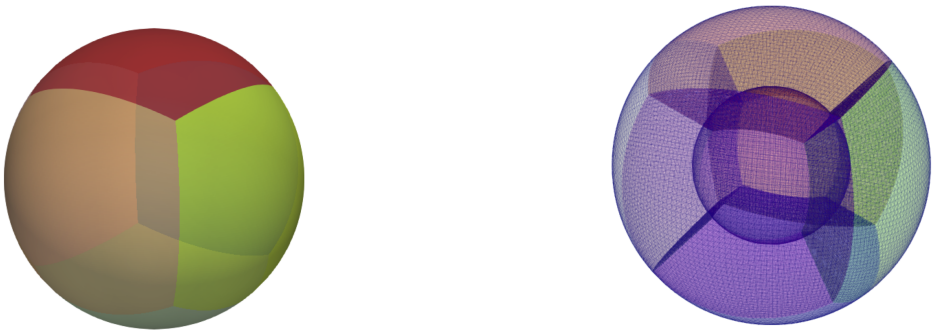

(a) IGA-PR-OSRC - multi-patch sphere model

(b) IGA-FEMABC - multi-patch mesh between the two concentric spheres

Figure 16: (a): Only the scatterer surface is meshed in IGA-PR-OSRC reducing the space dimension by one, leading to an important mesh reduction and low computational times. (b): IGA-FEABC needs the 3D meshing between the two concentric spheres.

and compared with the accurate solution based on the combination of IGA and Wilcox's expansion ABC (Fig. 17b). The IGA-PR-OSRC results were found with basis order $p = 2$ and only nDOF $= 2 \times 296$ degrees of freedom for $k = 20$ and nDOF $= 2 \times 1016$ for $k = 40$. We fixed the rotation angle for the OSRC to $\alpha = 0.69$. The accuracy of the results increases with the frequency k. The RCS $=$ RCS$(\theta, 0)$ in the plane $(x_1, x_2, 0)$ computed by IGA-PR-OSRC

for $k = 20$ and $k = 40$ are shown in Figures 18a and 18b. For comparison, we also report the RCS for the exact solution related to the Mie series expansion.

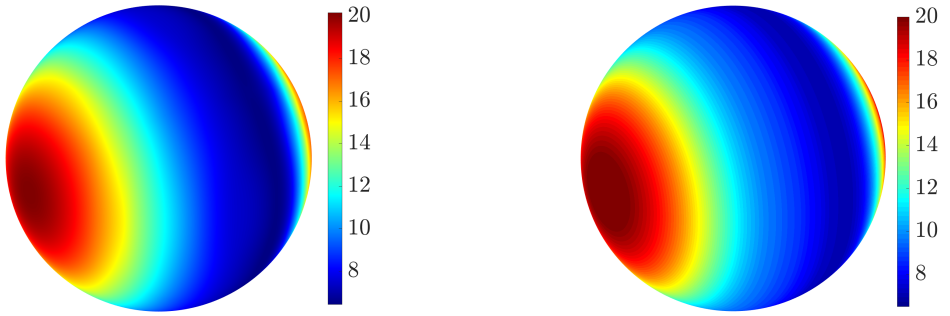

(a) IGA-PR-OSRC (b) IGA-FEABC

Figure 17: Amplitude of the normal derivative trace over the sphere based on IGA-PR-OSRC (a) and IGA-FEABC (b).

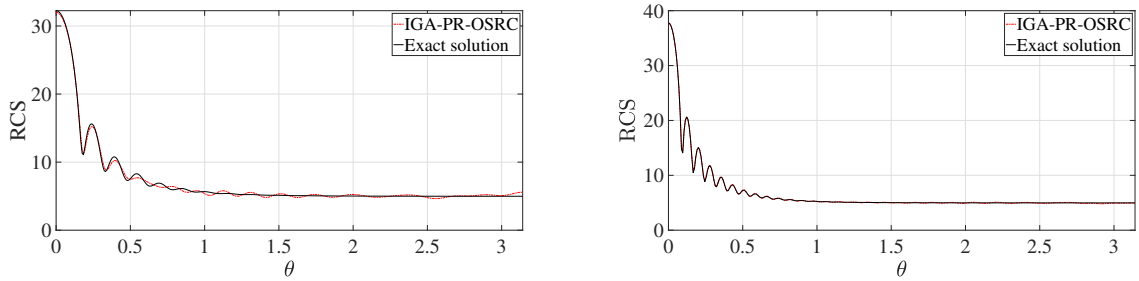

(a) RCS (dB): IGA-PR-OSRC - $k = 20$, nDOF $= 2 \times 296$. (b) RCS (dB): IGA-PR-OSRC - $k = 40$, nDOF $= 2 \times 1016$

Figure 18: RCS $=$ RCS$(\theta, 0)$ (dB) calculated for the sound-soft sphere by IGA-PR-OSRC and compared with exact solution for (a): $k = 20$ and (b): $k = 40$. The numerical results were obtained for the basis order $p = 2$ with nDOF $= 2 \times 296$ and nDOF $= 2 \times 1016$, respectively.

We next compare the RCS calculated by using IGA-PR-OSRC for the sound-hard sphere with the exact solution in Fig. 19. These results were obtained by considering the basis order $p = 2$, and nDOF $= 2 \times 1016$ degrees of freedom for both $k = 20$ and $k = 40$. The accuracy improves with the frequency without increasing the basis order p or the number of degrees of freedom nDOF. In terms of computational time, the resulting IGA-PR-OSRC method is extremely efficient and requires a very low memory storage.

To end, we consider the scattering problem by a sound-hard torpedo-shaped object (see Fig. 20a The plane wave is given by the parameter values $k = 20$ and $\theta^{\mathrm{i}} = 145°$. We report on Fig. 20b the amplitude of the surface field based on IGA-FEABC. Here, the basis order is $p = 5$ for nDOF $= 165,480$ to obtain the reference solution. We plot on Figures

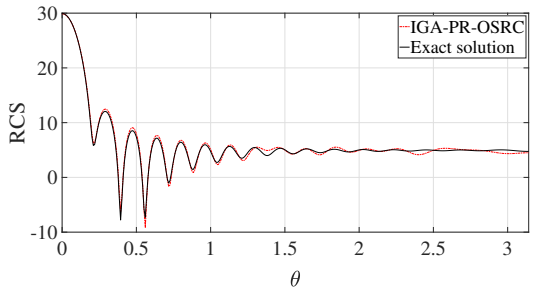

(a) RCS (dB): IGA-PR-OSRC - $k = 20$, nDOF $= 2 \times 1016$

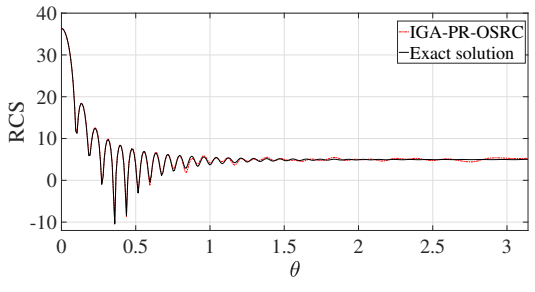

(b) RCS (dB): IGA-PR-OSRC - $k = 40$, nDOF $= 2 \times 1016$

Figure 19: RCS for the sound-hard unit sphere based on IGA-PR-OSRC and comparison with the exact solution for $k = 20$ and $k = 40$. The numerical results were computed for the basis order $p = 2$ with nDOF $= 2 \times 1016$.

20c and 20d the modulus of the trace computed by IGA-PR-OSRC for nDOF $= 2 \times 200$ and nDOF $= 2 \times 12728$, respectively. We observe a relatively good agreement, even for a very small number of degrees of freedom. Some accuracy is lost but this is mainly due to a lack of modelling of the OSRC operator in the case of the presence of a non convex part in the scatterer. Getting such a solution is however obtained extremely fast with low memory requirement. Increasing the accuracy for non convex obstacles will be studied in a future work. Finally, we report on Fig. 21a the related RCS in the plane $\{x_2 = 0\}$, i.e. in the slice along the longitudinal axis. We observe that a good estimation of the RCS is found using only nDOF $= 2 \times 200$ degrees of freedom. The comparison is made with the reference RCS computed with IGA-FEABC. We note that higher accuracy is expected for larger frequencies. We finally increase the number of degrees of freedom to nDOF $= 2 \times 12728$ and report the RCS on Figure 21b. We remark then that the improvement of the RCS calculation is not significant.

7. Conclusion

In this paper, we developed the NURBS-based IGA of both standard and Phase-Reduction OSRC formulations for 2D/3D acoustic scattering problems. In this framework, a Padé-type OSRC is analyzed and its tuning parameters are fixed by a numerical study. The case of a circular cylinder is fully investigated for both Dirichlet and Neumann boundary conditions. It appears that IGA allows to reduce greatly the number of discretization points of the method resulting in the IGA-OSRC method. In addition, using the Phase Reduction based on the plane wave ansatz, also leads to diminishing the number of points. This last method, called IGA-PR-OSRC, is then applied to a few more complicate two-dimensional scatterers, and simple three-dimensional shapes to validate the methodology. The resulting IGA-OSRC and IGA-PR-OSRC can serve later as interesting tools to improve more standard formulations for acoustic scattering solved by volume or surface integral formulations and approximated by IGA. Finally, the way to improve the accuracy of the method for non convex scatterers will be prospected in further works.

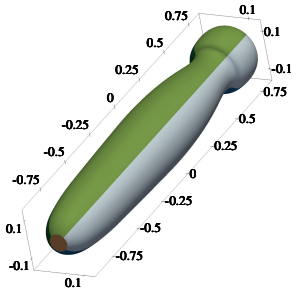

(a) The multi-patch torpedo-shaped model

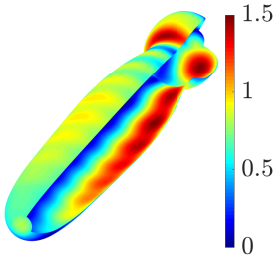

(b) IGA-FEABC solution

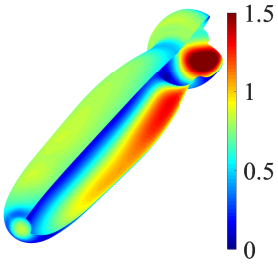

(c) PR-IGA-OSRC solution (nDOF $= 2 \times 200$)

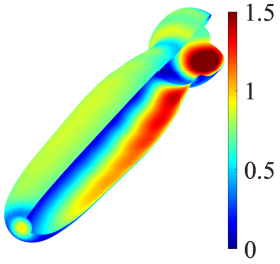

(d) PR-IGA-OSRC solution (nDOF $= 2 \times 12728$)

Figure 20: The modulus of the trace calculated for $k = 20$ and $\theta^{\mathrm{i}} = 145°$ using IGA-PR-OSRC is compared to the IGA-FEABC solution for a sound-hard torpedo shaped model. The IGA-PR-OSRC analysis was performed for the basis order $p = 2$ using (c) nDOF $= 2 \times 200$ (d) and nDOF $= 2 \times 12728$.

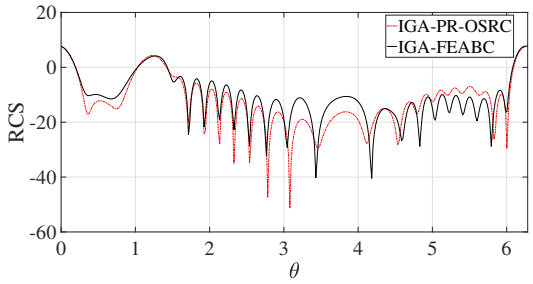

(a) RCS (dB): IGA-PR-OSRC - $k = 20$, nDOF $= 2 \times 200$

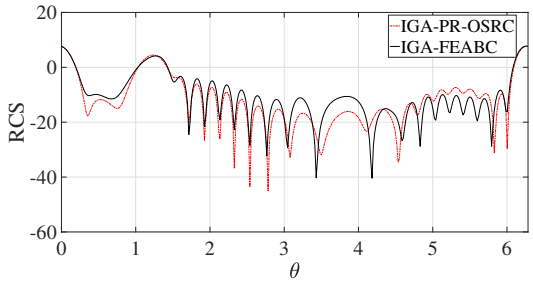

(b) RCS (dB): IGA-PR-OSRC - $k = 20$, nDOF $= 2 \times 12728$

Figure 21: RCS for the sound-hard torpedo based on IGA-PR-OSRC and comparison with the IGA-FEABC solution for $k = 20$ and $\theta^{\mathrm{i}} = 145°$. The numerical results were computed for the basis order $p = 2$ with nDOF $= 2 \times 200$, and nDOF $= 2 \times 12728$ respectively.

References

[1] S. Acosta. On-surface radiation condition for multiple scattering of waves. *Computer Methods in Applied Mechanics and Engineering*, 283:1296–1309, 2015.

[2] H. Alzubaidi, X. Antoine, and C. Chniti. Formulation and accuracy of on-surface radiation conditions for acoustic multiple scattering problems. *Applied Mathematics and Computation*, 277:82–100, 2016.

[3] H. Ammari and S. He. An on-surface radiation condition for Maxwell's equations in three dimensions. *Microwave and Optical Technology Letters*, 19(1):59–63, 1998.

[4] X. Antoine. Fast approximate computation of a time-harmonic scattered field using the on-surface radiation condition method. *IMA Journal on Applied Mathematics*, 66:83–110, 2001.

[5] X. Antoine. Advances in the On-Surface Radiation Condition Method: Theory, Numerics and Applications. In F. Magoulès, editor, *Computational Methods for Acoustics Problems*, pages 207–232. Saxe-Coburg Publishing Stirlingshire, UK, 2008.

[6] X. Antoine, H. Barucq, and A. Bendali. Bayliss-Turkel like radiation conditions on surfaces of arbitrary shape. *Journal of Mathematical Analysis and Applications*, 229:184–211, 1999.

[7] X. Antoine and M. Darbas. Alternative integral equations for the iterative solution of acoustic scattering problems. *The Quarterly Journal of Mechanics and Applied Mathematics*, 58(1):107–128, 2005.

[8] X. Antoine and M. Darbas. Generalized combined field integral equations for the iterative solution of the three-dimensional Helmholtz equation. *ESAIM: Mathematical Modelling and Numerical Analysis*, 41:147–167, 2007.

[9] X. Antoine and M. Darbas. An introduction to operator preconditioning for the fast iterative integral equation solution of time-harmonic scattering problems. *Multiscale Science and Engineering (https://doi.org/10.1007/s42493-021-00057-6)*, 2021.

[10] X. Antoine, M. Darbas, and Y.Y. Lu. An improved surface radiation condition for high-frequency acoustic scattering problems. *Computer Methods in Applied Mechanics and Engineering*, 195:4060–4074, 2006.

[11] X. Antoine and C. Geuzaine. Phase reduction models for improving the accuracy of the finite element solution of time-harmonic scattering problems I: General approach and low-order models. *Journal of Computational Physics*, 228(8):3114–3136, 2009.

[12] X. Antoine and C. Geuzaine. Optimized Schwarz Domain Decomposition Methods for Scalar and Vector Helmholtz Equations. In J. Tang D. Lahaye and K. Vuik, editors, *Modern Solvers for Helmholtz Problems*, pages 189–213. Birkhauser (Basel), 2017.

[13] R.J. Astley. Wave envelope and infinite elements for acoustical radiation. *International Journal for Numerical Methods in Fluids*, 3(5):507–526, 1983.

[14] A. Atle and B. Engquist. On surface radiation conditions for high-frequency wave scattering. *Journal of Computational and Applied Mathematics*, 204:306–316, 2007.

[15] E. Atroshchenko, A. Calderon Hurtado, C. Anitescu, and T. Khajah. Isogeometric collocation for acoustic problems with higher-order boundary conditions. *Submitted - Wave Motion*, 2020.

[16] A. Bayliss, M. Gunzburger, and E. Turkel. Boundary conditions for the numerical solution of elliptic equations in exterior regions. *SIAM Journal on Applied Mathematics*, 42:430–451, 1982.

[17] A. Bayliss and E. Turkel. Radiation boundary conditions for wave-like equations. *Communications on Pure and Applied Mathematics*, 33:707–725, 1980.

[18] J.P. Bérenger. A perfectly matched layer for the absorption of electromagnetic waves. *Journal of Computational Physics*, 114:185–200, 1994.

[19] A. Bermudez, L. Hervella-Nieto, A. Prieto, and R. Rodriguez. An optimal perfectly matched layer with unbounded absorbing function for time-harmonic acoustic scattering problems. *Journal of Computational Physics*, 223:469–488, 2007.

[20] A. Bermudez, L. Hervella-Nieto, A. Prieto, and R. Rodriguez. Perfectly matched layers for time-harmonic second order elliptic problems. *Archives for Computational Methods in Engineering*, 17:77–107, 2010.

[21] S. Börm, L. Grasedyck, and W. Hackbusch. Introduction to hierarchical matrices with applications. *Engineering Analysis with Boundary Elements*, 5(27):405–422, 2003.

[22] Y. Boubendir, X. Antoine, and C. Geuzaine. A quasi-optimal non-overlapping domain decomposition algorithm for the Helmholtz equation. *Journal of Computational Physics*, 231(2):262–280, 2012.

[23] Ph. Bouillard and F. Ihlenburg. Error estimation and adaptivity for the finite element method in acoustics: 2D and 3D applications. *Computer Methods in Applied Mechanics and Engineering*, 176(1):147–163, 1999.

[24] O.P. Bruno, C. Geuzaine, J.A. Monro, and F. Reitich. Prescribed error tolerances within fixed computational times for scattering problems of arbitrarily high frequency: the convex case. *Philosophical Transactions of the Royal Society of London A: Mathematical, Physical and Engineering Sciences*, 362(1816):629–645, 2004.

[25] W.C. Chew, J.M. Jin, E. Michielssen, and J. Song. *Fast and Efficient Algorithms in Computational Electromagnetics*. Artech House Antennas and Propagation Library, Norwood, 2001.

[26] R. Coifman, V. Rokhlin, and S. Wandzura. The Fast Multipole Method for the wave equation: A pedestrian description. *IEEE Transactions on Antennas and Propagation*, 3(35):7–12, 1993.

[27] F. Collino and P. Monk. The perfectly matched layer in curvilinear coordinates. *SIAM Journal on Scientific Computing*, 19:2061–2090, 1998.

[28] D. Colton and R. Kress. *Integral Equation Methods in Scattering Theory*. Wiley, 1983.

[29] L. Coox, O. Atak, D. Vandepitte, and W. Desmet. An isogeometric indirect boundary element method for solving acoustic problems in open-boundary domains. *Computer Methods in Applied Mechanics and Engineering*, 316:186–208, 2017.

[30] P. Costantini, C. Manni, F. Pelosi, and M.L. Sampoli. Quasi-interpolation in isogeometric analysis based on generalized b-splines. *Computer Aided Geometric Design*, 27(8):656 – 668, 2010. Advances in Applied Geometry.

[31] J.A. Cottrell, T.J.R. Hughes, and Y. Bazilevs. *Isogeometric Analysis: Toward Integration of CAD and FEA*. Wiley Publishing, 1st edition, 2009.

[32] J.A. Cottrell, A. Reali, Y. Bazilevs, and T.J.R. Hughes. Isogeometric analysis of structural vibrations. *Computer Methods in Applied Mechanics and Engineering*, 195(41-43):5257–5296, 2006.

[33] A. Deaño, D. Huybrechs, and A. Iserles. *Computing Highly Oscillatory Integrals*. SIAM, 2017.

[34] M. Dinachandra and R. Sethuraman. Plane wave enriched Partition of Unity Isogeometric Analysis (PUIGA) for 2D-Helmholtz problems. *Computer Methods in Applied Mechanics and Engineering*, 335:380–402, 2018.

[35] G.C. Diwan and M.S. Mohamed. Pollution studies for high order isogeometric analysis and finite element for acoustic problems. *Computer Methods in Applied Mechanics and Engineering*, 350:701–718, 2019.

[36] R. Djellouli, C. Farhat, A. Macedo, and R. Tezaur. Finite element solution of two dimensional scattering using arbitrarily shaped convex artificial boundaries. *Journal of Computational Acoustics*, 8(1):81–99, 2000.

[37] S.M. Dsouza, T. Khajah, X. Antoine, S.P.A. Bordas, and S. Natarajan. Non Uniform Rational B-Splines and Lagrange approximations for time-harmonic acoustic scattering: accuracy and absorbing boundary conditions. *Mathematical and Computer Modelling of Dynamical Systems*, 2021, to appear.

[38] J. Dölz, H. Harbrecht, S. Kurz, S. Schöps, and F. Wolf. A fast isogeometric BEM for the three dimensional Laplace- and Helmholtz problems. *Computer Methods in Applied Mechanics and Engineering*, 330:83–101, 2018.

[39] B. Engquist and A. Majda. Absorbing boundary conditions for the numerical simulation of waves. *Mathematics of Computation*, 31:629–651, 1977.

[40] Y. Erlangga. Advances in iterative methods and preconditioners for the Helmholtz equation. *Archives for Computational Methods in Engineering*, 15:37–66, 2008.

[41] O. Ernst and M.J. Gander. Why it is Difficult to Solve Helmholtz Problems with Classical Iterative Methods. In O. Lakkis I. Graham, T. Hou and R. Scheichl, editors, *Numerical Analysis of Multiscale Problems*, pages 325–363. Springer Verlag, 2012.

[42] M.J. Gander, F. Magoulès, and F. Nataf. Optimized Schwarz methods without overlap for the Helmholtz equation. *SIAM Journal on Scientific Computing*, 24(1):38–60, 2002.

[43] C. Geuzaine, J. Bedrossian, and X. Antoine. An amplitude formulation to reduce the pollution error in the finite element solution of time-harmonic scattering problems. *IEEE Transactions on Magnetics*, 44(6):782–785, June 2008.

[44] E. Giladi and J.B. Keller. A hybrid numerical asymptotic method for scattering problems. *Journal of Computational Physics*, 174(1):226–247, 2001.

[45] D. Givoli. High-order local non-reflecting boundary conditions : a review. *Wave Motion*, 39:319–326, 2004.

[46] L. Greengard and V. Rokhlin. A fast algorithm for particle simulations. *Journal of Computational Physics*, 2(73):325–348, 1987.

[47] W. Hackbusch. *Hierarchical Matrices: Algorithms and Analysis*, volume 49. Springer Series in Computational Mathematics, Springer, Heidelberg, 2015.

[48] T.J.R. Hughes, J.A. Cottrell, and Y. Bazilevs. Isogeometric analysis: CAD, Finite Elements, NURBS, exact geometry and mesh refinement. *Computer Methods in Applied Mechanics and Engineering*, 194(39-41):4135–4195, 2005.

[49] T.J.R. Hughes, J.A. Evans, and A. Reali. Finite element and NURBS approximations of eigenvalue, boundary-value, and initial-value problems. *Computer Methods in Applied Mechanics and Engineering*, 272:290–320, 2014.

[50] F. Ihlenburg. *Finite Element Analysis of Acoustic Scattering*. Springer, 1998.

[51] F. Ihlenburg and I. Babuška. Finite element solution of the Helmholtz equation with high wave number Part I: The h-version of the FEM. *Computers and Mathematics with Applications*, 30(9):9–37, 1 1995.

[52] F. Ihlenburg and I. Babuska. Finite element solution of the Helmholtz equation with high wave number Part II: the h-p version of the FEM. *SIAM Journal on Numerical Analysis*, 34(1):315–358, February 1997.

[53] R. Kechroud, A. Soulaimani, Y. Saad, and S. Gowda. Preconditioning techniques for the solution of the Helmholtz equation by the finite element method. *Mathematics and Computers in Simulation*, 65:303–321, 2004.

[54] T. Khajah, X. Antoine, and S.P.A. Bordas. B-spline FEM for time-harmonic acoustic scattering and propagation. *Journal of Theoretical and Computational Acoustics*, 2019.

[55] T. Khajah and V. Villamizar. Highly accurate acoustic scattering: Isogeometric analysis coupled with local high order farfield expansion ABC. *Computer Methods in Applied Mechanics and Engineering*, 349:477–498, 2019.

[56] S. Kirkup. The Boundary Element Method in acoustics: a survey. *Applied Sciences-Basel*, 8(9), 2019.

[57] F. Kpadonou, S. Chaillat, and P. Ciarlet. On the efficiency of nested GMRES preconditioners for 3D acoustic and elastodynamic H-matrix accelerated Boundary Element Methods. *Computers and Mathematics with Applications*, 3(80):471–489, 2020.

[58] G. Kriegsmann, A. Taflove, and K. Umashankar. A new formulation of electromagnetic wave scattering using an on-surface radiation boundary condition approach. *IEEE Transactions on Antennas and Propagation*, 35(2):153–161, 1987.

[59] O. Laghrouche and P. Bettess. Short wave modelling using special finite elements. *Journal of Computational Acoustics*, 08(01):189–210, 2000.

[60] O. Laghrouche, P. Bettess, and R.J. Astley. Modelling of short wave diffraction problems using approximating systems of plane waves. *International Journal for Numerical Methods in Engineering*, 54(10):1501–1533, 2002.

[61] O. Laghrouche, A. El-Kacimi, and J. Trevelyan. A comparison of NRBCs for PUFEM in 2D Helmholtz problems at high wave numbers. *Journal of Computational and Applied Mathematics*, (6):1670–1677. Eighth International Conference on Mathematical and Numerical Aspects of Waves (Waves 2007).

[62] M. Medvinsky and E Turkel. On surface radiation conditions for an ellipse. *Journal of Computational and Applied Mathematics*, 234(6):1647–1655, 2010.

[63] M. Medvinsky, E. Turkel, and U. Hetmaniuk. Local absorbing boundary conditions for elliptical shaped boundaries. *Journal of Computational Physics*, 227:8254–8267, 2008.

[64] J.C. Nédélec. *Acoustic and Electromagnetic Equations : Integral Representations for Harmonic Problems*. Springer, 2001.

[65] V.P. Nguyen, C. Anitescu, S.P.A. Bordas, and T. Rabczuk. Isogeometric analysis: An overview and computer implementation aspects. *Mathematics and Computers in Simulation*, 117:89–116, 2015.

[66] N. Nguyen-Thanh, K. Zhou, X. Zhuang, P. Areias, H. Nguyen-Xuan, Y. Bazilevs, and T. Rabczuk. Isogeometric analysis of large-deformation thin shells using RHT-splines for multiple-patch coupling. *Computer Methods in Applied Mechanics and Engineering*, 316:1157–1178, 2017. Special Issue on Isogeometric Analysis: Progress and Challenges.

[67] M.J. Peake, J. Trevelyan, and G. Coates. Extended isogeometric boundary element method (XIBEM) for two-dimensional Helmholtz problems. *Computer Methods in Applied Mechanics and Engineering*, 259:93–102, 2013.

[68] M.J. Peake, J. Trevelyan, and G. Coates. Extended isogeometric boundary element method (XIBEM) for three-dimensional medium-wave acoustic scattering problems. *Computer Methods in Applied Mechanics and Engineering*, 284:762–780, 2015.

[69] D. Rabinovich, D. Givoli, J. Bielak, and T. Hagstrom. A finite element scheme with a high order absorbing boundary condition. *Computer Methods in Applied Mechanics and Engineering*, 200:2048–2066, 2011.

[70] V. Rokhlin. Rapid solution of integral equations of scattering theory in two dimensions. *Journal of Computational Physics*, 2(86):414–439, 1990.

[71] S. J. Sherwin and J. Peiró. Mesh generation in curvilinear domains using high-order elements. *International Journal for Numerical Methods in Engineering*, 53(1):207–223, 2002.

[72] R.N. Simpson, M.A. Scott, M. Taus, D.C. Thomas, and H. Lian. Acoustic isogeometric boundary element analysis. *Computer Methods in Applied Mechanics and Engineering*, 269:265–290, 2014.

[73] R. Tezaur, A. Macedo, C. Farhat, and R. Djellouli. Three-dimensional finite element calculations in acoustic scattering using arbitrarily shaped convex artificial boundaries. *International Journal forr Numerical Methods in Engineering*, 53:1461–1476, 2002.

[74] S. Tsynkov. Numerical solution of problems on unbounded domains. *Applied Numerical Mathematics*, 27:465–532, 1998.

[75] E. Turkel, C. Farhat, and U. Hetmaniuk. Improved accuracy for the Helmholtz equation in unbounded domains. *International Journal for Numerical Methods in Engineering*, 59(15):1963–1988, 2004.

[76] E. Turkel and A. Yefet. Absorbing PML boundary layers for wave-like equations. *Applied Numerical Mathematics*, 27:533–557, 1998.

[77] J.V. Venås and T. Kvamsdal. Isogeometric boundary element method for acoustic scattering by a submarine. *Computer Methods in Applied Mechanics and Engineering*, 359:112670, 2020.

[78] J.V. Venås, T. Kvamsdal, and T. Jenserud. Isogeometric analysis of acoustic scattering using infinite elements. *Computer Methods in Applied Mechanics and Engineering*, 335:152–193, 2018.

[79] J. Videla, C. Anitescu, T. Khajah, S.P.A. Bordas, and E. Atroshchenko. h- and p-adaptivity driven by recovery and residual-based error estimators for PHT-splines applied to time-harmonic acoustics. *Computers and Mathematics with Applications*, 77(9):2369–2395, 2019.

[80] V. Villamizar, S. Acosta, and B. Dastrup. Exact local absorbing boundary conditions for time-harmonic waves in terms of farfield expansions. *Journal of Computational Physics*, 333:331–351, 2017.

[81] W.A. Wall, M.A. Frenzel, and C. Cyron. Isogeometric structural shape optimization. *Computer Methods in Applied Mechanics and Engineering*, 197(33-40):2976–2988, 2008.

[82] T. Wu. A dispersion minimizing compact finite difference scheme for the 2D Helmholtz equation. *Journal of Computational and Applied Mathematics*, 311:497–512, 2017.

[83] Y.H. Wu, C.Y. Dong, and H.S. Yang. Isogeometric indirect boundary element method for solving the 3D acoustic problems. *Journal of Computational and Applied Mathematics*, 363:273–299, 2020.

[84] G. Xu, B. Li, L. Shu, L. Chen, J. Xu, and T. Khajah. Efficient r-adaptive isogeometric analysis with winslow's mapping and monitor function approach. *Journal of Computational and Applied Mathematics*, 351:186–197, 2019.